Magnetic-field-engineered coherent perfect absorption and transmission

Zhiming Wu,[*] Jiahua Li [ORCID],[†] and Ying Wu[‡]

School of Physics, Huazhong University of Science and Technology, Wuhan 430074, People's Republic of China

An experimental work [W. J. Wan, Y. D. Chong, L. Ge, H. Noh, A. D. Stone, and H. Cao, Science **331**, 889 (2011)] showed that a resonator that contains a loss medium instead of a gain medium enables coherent perfect absorption (CPA) by interference. Here, we propose an alternative approach to realize such a CPA and coherent perfect transmission (CPT) as well as the switching between CPA and CPT in a cavity quantum electrodynamics (CQED) system by applying an external magnetic field. The proposed CPA and CPT scheme is based on the magnetically induced transparency (MIT) configuration, instead of the conventional electromagnetically induced transparency configuration, which offers a sensitive method to tune CPA and CPT and also is conducive to the flexible control of the CPA and CPT scheme. Under the linear and nonlinear excitation regimes, we derive the approximate analytical solutions of the cavity-output power and the CPA criteria of the CQED system, and find that the CPA can occur at different frequencies in both regimes. In the nonlinear excitation regime, the relationship between the cavity-output power and the cavity-input power can show a bistable characteristic by the control of the static magnetic field, and the CPA point is near the turning point of the cavity-input power on the bistable return hysteresis curve. Furthermore, the line shape and the threshold value for optical bistability can be flexibly controlled by varying the magnetic field under experimentally accessible conditions, thus the magnetic field can well tune the CPA. Also, we compare the analytical and numerical results of the cavity-output power in the nonlinear excitation regime, and they are in good agreement. Our results show that the CQED system based on the MIT configuration can be used as a perfect absorber or nearly perfect transmitter, which may have practical applications in optical logic and optical communication devices.

I. INTRODUCTION

Besides reflection and refraction, absorption is a general phenomenon of the coherent interaction between light and matter, which is significant for a variety of fundamental studies and practical applications [1–8]. In recent years, coherent perfect absorption (CPA) that arises from the interference of two coherent counterpropagating light fields in a confined cavity structure has attracted tremendous research interests [9–12]. So far, the CPA has been proposed theoretically in several systems, including metasurfaces [5,13–15], gratings [16–18], graphenes [19,20], photonic crystals [21,22], optical cavities [23,24], and so on. In particular, the CPA has been studied in optical Fabry-Pérot cavities containing metamaterials [15,25–27], loss media [2], planar slabs [28,29], thin films [5,30–33], and optical waveguides [34,35]. Such a cavity-absorber system can be used as a coherent perfect absorber and may have potential applications in information communication [36,37], all-optical switching [38], signal modulation [39,40], acoustic absorption [41], optical logical devices [42,43], etc.

In 2011, Wan *et al.* observed experimentally that, in the time-reversed counterpart to laser emission, the CPA can be achieved in a dissipative silicon cavity [3]. Also similar CPA with two coherent input light fields is manipulated by electromagnetically induced transparency (EIT) in a cavity quantum electrodynamics (CQED) system, which has received a lot of attention [10,44–48]. For the conventional EIT in atomic systems, the atom is generally modeled as a three-level system, in which the light at one frequency from a strong control laser renders a medium transparent to the light from a weak probe laser at a second frequency. In particular, in the CPA scheme based on the EIT configuration, one can use the additional control laser to modify the interaction between the cavity and the atoms, and then realize the CPA. With the EIT-type quantum interference induced by the control laser, the light fields coupled to the optical cavity can be completely absorbed, and no light can escape through the cavity, i.e., the so-called CPA is achieved.

In analogy to EIT, a phenomenon called magnetically induced transparency (MIT) gives access to the essential features of EIT, but it only needs a static magnetic field instead of an additional control laser to change the properties of the medium [49–60]. Here we put forward an alternative route to realize the CPA and coherent perfect transmission (CPT) as well as the switching between CPA and CPT by simply employing the Faraday magnetic field in a CQED system, instead of the strong control field in the conventional EIT system. Specifically, the proposed CQED system consists of an optical Fabry-Pérot cavity containing N three-level V-type atoms [with two closely lying upper states $|1\rangle$ and $|2\rangle$, and one

---

[*]zhiming@hust.edu.cn
[†]Corresponding author: huajia_li@126.com
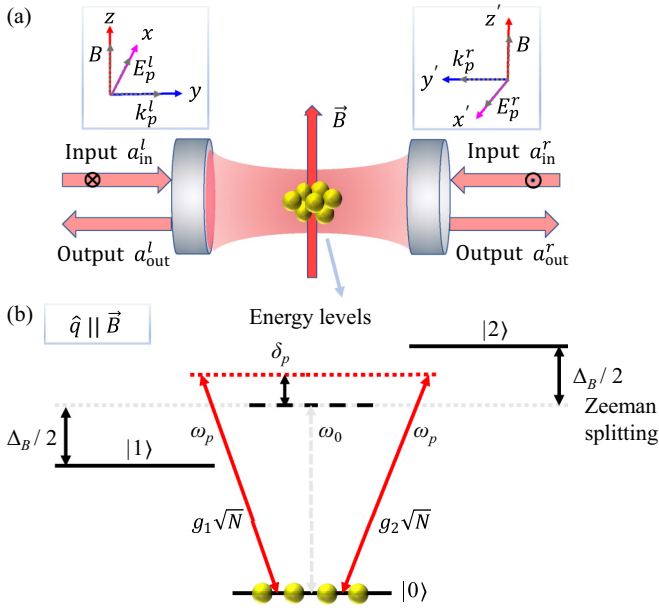[‡]yingwu2@126.com

FIG. 1. (a) Schematic of the CQED system. The CQED system consists of N three-level V-type atoms (the small golden filled circles) confined in the cavity mode, which are subject to a Faraday magnetic field B. Two horizontally polarized input light fields (a_{in}^l and a_{in}^r) are coupled into the cavity from opposite ends. The magnetic field is applied along the vertical direction, which interacts with the atoms from the open side of the cavity. The two top insets illustrate the relative orientation of the input-light polarization (E_p^l and E_p^r), the input-light propagation (k_p^l and k_p^r), and the Faraday magnetic field (B). (b) Energy-level structure of the atoms in the presence of an external magnetic field applied in the Faraday geometry. The ground state is denoted by $|0\rangle$ and the two bright excited states are represented by $|1\rangle$ and $|2\rangle$. The quantization axis $\hat{q}$ of the atomic energy level is parallel to the applied magnetic field B and the applied magnetic field creates a Zeeman splitting Δ_B between the excited states $|1\rangle$ and $|2\rangle$. Four small golden filled circles represent schematically that the atomic population is concentrated in the ground state $|0\rangle$. The left (right) horizontally polarized input light field (which is considered as a superposition of the σ^- and σ^+ components) with the angular frequency ω_p and the amplitude E_p^l (E_p^r) which polarizes along the x (x') axis and propagates along the y (y') axis is applied to coherently drive the cavity mode with the resonance frequency ω_c and to couple both the $|1\rangle \leftrightarrow |0\rangle$ excited transition with the excited resonance frequency ω_{10} and the $|2\rangle \leftrightarrow |0\rangle$ excited transition with the excited resonance frequency ω_{20}. Other symbols are defined in the text.

ground state $|0\rangle$; see Fig. 1(b)], which are subject to a Faraday magnetic field and are excited by two horizontally polarized input light fields from two opposite ends of the cavity. We find that the applied magnetic field plays an important role in modifying the photon output properties of the system. By simply turning the magnetic field on or off, the CQED system can act as a perfect absorber or perfect transmitter at multiple input light frequencies instead of only one single frequency [48]. This means that the CPA criterion is easier to be satisfied under the control of magnetic field. Alternatively, the CPA can be tuned from the linear excitation regime into the nonlinear excitation regime by varying the cavity-input power. By analyzing the steady state of the photon-atom interactions in the

CQED system, we can derive the cavity-output power from the two partially transmitting cavity mirrors in the linear and nonlinear excitation regimes. Our results show that the CPA can occur in both linear and nonlinear excitation regimes of the CQED system. We also derive the analytical expressions of the CPA based on the MIT configuration and the analytical results are in good agreement with the numerical simulations. In the linear excitation regime, the control of the magnetic field can realize the conversion of the CQED system from a perfect photon absorber to a perfect photon transmitter, i.e., the cavity output is capable of switching from CPA to CPT or vice versa. In the nonlinear excitation regime, the relationship between the cavity-output power and the cavity-input power can show a bistable characteristic by the control of the static magnetic field, and the CPA point is near the turning point of the cavity-input power on the bistable return hysteresis curve. We also illustrate the phase dependence of the CPA, and especially show the effect of interference on optical bistability of the CQED system. The bistability can be well controlled by simply varying the magnetic field and the relative phase of the two input fields, which has potential applications based on optical bistability such as optical switching and optical multiplexing [61–63]. Also, we demonstrate that this scheme of CPA and CPT can be implemented based on a real physical platform.

Compared with the schemes proposed in Refs. [12,47,48,64], the present paper contains three major advantages.

(i) Unlike the scheme based on the EIT configuration that responds to only a specific input light frequency [48], the scheme based on the MIT configuration can realize the conversion between the CPA and CPT at multiple input light frequencies at the same time, which relaxes the frequency requirements in the previous scheme based on the EIT configuration.

(ii) The introduction of an external, static magnetic field provides an additional degree of freedom (a tuning parameter) by which the CPA can be controlled. Under the control of the magnetic field, the CQED system can realize the conversion between the CPA and CPT without the need for changing the optical characteristics (i.e., the phase and frequency) of the absorbed lights [12]. That is to say, it is not necessary to change the phase and frequency of the absorbed lights to realize the conversion between complete absorption and complete transmission, just replaced by simply turning the external magnetic field on or off, which relax the requirement for the absorbed lights. Moreover, our scheme shows that tuning the magnetic field is beneficial for the absorption of stronger input lights than tuning the collective cavity-atom coupling strength. This possibility of active control of the CPA opens up an alternative idea for potential applications [26,38].

(iii) The CPA is robust to the variation of the magnetic field when the magnetic-field strength is near zero in our scheme based on MIT configuration, which may make it reliable to use the magnetic field as a switching parameter from the CPA to the CPT.

On the other hand, it is worth pointing out that our magnetic-field-engineered CPA and CPT scheme is fundamentally different from the previous methods utilizing an EIT [10,47,48], where the control-light-based EIT architecture (in-

volving detuning, polarization, wave-vector matching, etc.) is needed. To some extent our scheme proposed here makes the experimental realization more friendly. The CPA is an interference phenomenon in which the light fields incident on a lossy medium are completely absorbed by the medium through the process of destructive interference among all scattering amplitudes [65–72]. The captured light is then converted to other forms of energy inside the medium such as electrical energy or heat. The CPA is a material independent phenomenon and typically hinges on maintaining correct phases and amplitudes of the incident light beams. In principle, CPA has been generalized to diverse types of materials and has been reported to be attained in the generic type of complex scattering structures with and without hidden symmetries [73]. These motivate us to further explore CPA in the CQED setup by engineering the static magnetic field. In the previous works on MIT, Gevorgyan investigated the application of MIT in an ideal optical diode [54], and Winchester *et al.* demonstrated a technique to realize a narrow spectroscopic feature based on MIT [74]. Differently from Refs. [54,74], the present paper mainly focuses on the conversion between the CPA and CPT in the linear and nonlinear regimes, which is useful for designing all-optical switchings [38] and logic elements [26].

The subsequent sections are organized as follows. In Sec. II, we describe the theoretical model and the Hamiltonian of the CQED system, then derive the process of cavity-output and cavity-inside powers. In Sec. III, we demonstrate the experimental feasibility of our proposed CPA and CPT scheme and the choice of typical CQED system parameters. All parameters discussed here are readily achievable experimentally. In Sec. IV, we devote ourselves to identifying the CPA in the linear excitation regime and describe in detail the switching of the CQED system from a perfect photon absorber to a nearly perfect photon transmitter based on the MIT configuration. The analytical results and criteria of the CPA are given and discussed. In Sec. V, we analyze the CPA in the nonlinear excitation regime. The relationship between the cavity-output power and the cavity-input power can show an optical bistability, where optical bistability can be turned on or off under the control of the applied magnetic field, and can be manipulated by varying the relative phase of the two input fields. Finally, the paper is summarized in Sec. VI.

II. PHYSICAL SYSTEM AND THEORETICAL FRAMEWORK

Figure 1 shows the schematic diagram for a coupled CQED system that consists of N three-level V-type atoms inside in a single-mode cavity, which are subject to a Faraday magnetic field B. The CQED system is excited by two horizontally polarized input light fields ($a_{\rm in}^l$ and $a_{\rm in}^r$) from two opposite ends of the cavity. The relative orientations of the input-light polarization (E_p^l and E_p^r), the input-light propagation (k_p^l and k_p^r), and the Faraday magnetic field (B) are depicted in the two top insets in Fig. 1(a). The left (right) input light field polarizes along the x (x') axis and propagates along the y (y') axis. The magnetic field is applied along the z axis (the z axis and the z' axis are in the same direction), which interacts with the atoms from the open side of the cavity and induces a Zeeman

splitting between the upper energy levels $|1\rangle$ and $|2\rangle$. Here, the atoms are regarded as a three-level V-type system [74] with a ground state $|0\rangle$ and two upper bright excited states $|1\rangle$ and $|2\rangle$ in the presence of an external magnetic field applied in the Faraday geometry in which the magnetic field is parallel to the y-z plane [see Fig. 1(b) and Sec. III below for details]. The coherent interaction in such a coupled CQED system is described, in the presence of both the two input light fields and the Faraday magnetic field, by the total Hamiltonian $\hat{H}_{\rm tot} = \hat{H}_{a+c} + \hat{H}_i$, where $\hat{H}_{a+c}$ is the free Hamiltonian for the atoms and the cavity field and $\hat{H}_i$ is the interaction Hamiltonian for the coupled CQED system. Again, the free Hamiltonian $\hat{H}_{a+c}$ within the electric-dipole and rotating-wave approximations as well as in the Schrödinger picture reads (assuming the Hamiltonian will be taken to have units of frequency here and hereafter)

$$\hat{H}_{a+c} = \omega_c \hat{a}^\dagger \hat{a} + \sum_{i=1}^{N}(\omega_0 - \Delta_B/2)\hat{\sigma}_{11}^{(i)}$$
$$+ \sum_{i=1}^{N}(\omega_0 + \Delta_B/2)\hat{\sigma}_{22}^{(i)}, \qquad (1)$$

and the interaction Hamiltonian $\hat{H}_i$ reads

$$\hat{H}_i = \sum_{i=1}^{N} g_1 \hat{a}\hat{\sigma}_{10}^{(i)} + \sum_{i=1}^{N} g_2 \hat{a}\hat{\sigma}_{20}^{(i)}$$
$$+ i\hat{a}^\dagger e^{-i\omega_p t}\left(\sqrt{\kappa_l/\tau}\,a_{\rm in}^l + \sqrt{\kappa_r/\tau}\,a_{\rm in}^r\right) + \text{H.c.} \qquad (2)$$

Here, $\hat{a}^\dagger$ and $\hat{a}$ are the creation and annihilation operators for photons inside the cavity obeying the bosonic commutation relations $[\hat{a}, \hat{a}^\dagger] = 1$, $[\hat{a}^\dagger, \hat{a}^\dagger] = 0$ and $[\hat{a}, \hat{a}] = 0$. Δ_B is the Zeeman splitting between the two excited states $|1\rangle$ and $|2\rangle$ under the Faraday magnetic field [see Fig. 1(b)]. ω_c is the resonance frequency of the cavity mode. $\omega_0 = (\omega_{10} + \omega_{20})/2 = \omega_{10} + \Delta_B/2 = \omega_{20} - \Delta_B/2$ denotes the atomic transition frequency (in the limit of zero applied magnetic field, each atom can be regarded as a two-level system according to Ref. [74]), where ω_{10} (ω_{20}) is the excited resonance frequency for the $|0\rangle \leftrightarrow |1\rangle$ ($|0\rangle \leftrightarrow |2\rangle$) transition of the three-level atoms. $\hat{\sigma}_{lm}^{(i)} = |l\rangle\langle m|$ ($l, m = 0, 1, 2$) represents the raising ($l > m$), lowering ($l < m$), or population ($l = m$) operator for the ith atom. N is the number of the atoms inside the cavity. $g_1 = \mu_{01}\sqrt{\omega_c/(2\hbar\varepsilon_0 V)}$ and $g_2 = \mu_{02}\sqrt{\omega_c/(2\hbar\varepsilon_0 V)}$ are the cavity-atom coupling strengths for the transitions $|0\rangle \leftrightarrow |1\rangle$ and $|0\rangle \leftrightarrow |2\rangle$, respectively, where μ_{01} and μ_{02} are the electric-dipole moments of the corresponding transitions $|0\rangle \leftrightarrow |1\rangle$ and $|0\rangle \leftrightarrow |2\rangle$, $\hbar$ is the reduced Planck constant, ε_0 is the permittivity of vacuum, and V is the mode volume of the cavity. In accordance with the previous reports in Refs. [12,47,48,64], the coupling strengths g_1 and g_2 can be assumed to be uniform for the N identical atoms (i.e., $\hat{\sigma}_{lm}^{(i)} = \hat{\sigma}_{lm}$) inside the cavity. $a_{\rm in}^l$ and $a_{\rm in}^r$ are two input light fields to the cavity [see Fig. 1(a)]. The left (right) input light field is described by $\vec{\mathcal{E}}_p^l = \vec{e}_x E_p^l e^{-i\omega_p t}$ ($\vec{\mathcal{E}}_p^r = \vec{e}_{x'} E_p^r e^{-i\omega_p t}$) with its unit polarization vector $\vec{e}_x$ ($\vec{e}_{x'}$), amplitude E_p^l (E_p^r), and frequency ω_p (the two input light fields have the same frequency). $\kappa_l = T_l/\tau$ ($\kappa_r = T_r/\tau$) is the decay rate from the left (right) cavity mirror, with T_l

(T_r) being the left (right) cavity mirror transmission and τ the photon round-trip time inside the cavity [12,47,48,64,75]. We reasonably ignore the inner cavity damping rate because it is much smaller than that of the cavity mirror. H.c. denotes the Hermitian conjugate. Since the zero-point energy for the free Hamiltonian $\hat{H}_{a+c}$ only gives a relative shift without affecting the dynamics of the system, we can ignore the zero-point energy for the free Hamiltonian $\hat{H}_{a+c}$ and choose the ground-state energy as zero in Eq. (1).

For the sake of eliminating the explicit temporal dependence in the above Hamiltonian $\hat{H}_{\text{tot}}$, we would like to change $\hat{H}_{\text{tot}}$ into a rotating reference frame with respect to the input-light frequency ω_p by applying the unitary operator $\hat{U}(t) = \exp(-i\hat{H}_0 t)$, where $\hat{H}_0 = \omega_p(\hat{a}^\dagger \hat{a} + \sum_{i=1}^{N} \hat{\sigma}_{11}^{(i)} + \sum_{i=1}^{N} \hat{\sigma}_{22}^{(i)})$. Finally, in terms of the formula $\hat{H}_{\text{eff}} = \hat{U}^\dagger(t)\hat{H}_{\text{tot}}\hat{U}(t) - i\hat{U}^\dagger(t)\partial\hat{U}(t)/\partial t$ [76], we can derive a time-independent effective Hamiltonian of the CQED system after some algebra, with the form

$$
\hat{H}_{\text{eff}} = \sum_{i=1}^{N}(-\delta_p - \Delta_B/2)\hat{\sigma}_{11}^{(i)} + \sum_{i=1}^{N}(-\delta_p + \Delta_B/2)\hat{\sigma}_{22}^{(i)}
$$
$$
+ (\delta_c - \delta_p)\hat{a}^\dagger \hat{a} + \left\{ \sum_{i=1}^{N} g_1\hat{a}\hat{\sigma}_{10}^{(i)} + \sum_{i=1}^{N} g_2\hat{a}\hat{\sigma}_{20}^{(i)} \right.
$$
$$
\left. + i\hat{a}^\dagger\left(\sqrt{\kappa_r/\tau}a_{\text{in}}^r + \sqrt{\kappa_l/\tau}a_{\text{in}}^l\right) + \text{H.c.} \right\}, \quad (3)
$$

where the notation $\delta_p = \omega_p - \omega_0$ is the detuning of the input-light frequency ω_p from the atomic transition frequency ω_0. $\delta_c = \omega_c - \omega_0$ is the detuning of the resonance frequency ω_c of the cavity mode from the atomic transition frequency ω_0.

In order to describe the complete dynamics of the CQED system with the joint atom-cavity density matrix operator $\hat{\rho}$, we use the Lindblad master equation in the Born-Markov approximation [76–79]

$$
\frac{d\hat{\rho}}{dt} = -i[\hat{H}_{\text{eff}}, \hat{\rho}] + (\kappa_l + \kappa_r)\mathcal{D}(\hat{a})\hat{\rho}
$$
$$
+ \gamma_1 \mathcal{D}(\hat{\sigma}_{01})\hat{\rho} + \gamma_2 \mathcal{D}(\hat{\sigma}_{02})\hat{\rho}, \quad (4)
$$

with $\hat{H}_{\text{eff}}$ being the effective Hamiltonian directly yielded by Eq. (3) under the ω_p-rotating frame of the CQED system and the brackets $[\cdot, \cdot]$ denoting the commutator. $\mathcal{D}(\hat{O})\hat{\rho} = \hat{O}\hat{\rho}\hat{O}^\dagger - 1/2\hat{O}^\dagger\hat{O}\hat{\rho} - 1/2\hat{\rho}\hat{O}^\dagger\hat{O}$ is the general Lindblad operator form for the collapse operator $\hat{O}$, which is used to account for the dissipation to the environment. κ_l and κ_r are the decay rates of the left cavity mirror and right cavity mirror, respectively. γ_1 and γ_2 are the decay rates of the atoms for the $|1\rangle \leftrightarrow |0\rangle$ transition and $|2\rangle \leftrightarrow |0\rangle$ transition. We can ignore the quantum fluctuation terms and treat $\hat{\sigma}_{lm}$ $(l, m = 0, 1, 2)$ and $\hat{a}$ as c numbers (i.e., the mean-field approximation) in accordance with the previous reports in Refs. [12,47,48,64]. This approximation is valid for a large number of atoms in the cavity mode. Then, we can derive the resulting equations of motion of the CQED system for the expectation values of σ_{lm} $(l, m = 0, 1, 2)$ and a, which read

$$
\dot{\sigma}_{00} = \gamma_1\sigma_{11} + \gamma_2\sigma_{22} + ig_1 a\sigma_{10} + ig_2 a\sigma_{20} - ig_1^* a^\dagger \sigma_{01}
$$
$$
- ig_2^* a^\dagger \sigma_{02}, \quad (5)
$$

$$
\dot{\sigma}_{11} = -\gamma_1\sigma_{11} - ig_1 a\sigma_{10} + ig_1^* a^\dagger \sigma_{01}, \quad (6)
$$

$$
\dot{\sigma}_{22} = -\gamma_2\sigma_{22} - ig_2 a\sigma_{20} + ig_2^* a^\dagger \sigma_{02}, \quad (7)
$$

$$
\dot{\sigma}_{01} = [i(\delta_p + \Delta_B/2) - \gamma_1/2]\sigma_{01} + ig_1 a(\sigma_{11} - \sigma_{00})
$$
$$
+ ig_2 a\sigma_{21}, \quad (8)
$$

$$
\dot{\sigma}_{02} = [i(\delta_p - \Delta_B/2) - \gamma_2/2]\sigma_{02} + ig_2 a(\sigma_{22} - \sigma_{00})
$$
$$
+ ig_1 a\sigma_{12}, \quad (9)
$$

$$
\dot{\sigma}_{21} = (i\Delta_B - \gamma_1/2 - \gamma_2/2)\sigma_{21} - ig_1 a\sigma_{20}
$$
$$
+ ig_2^* a^\dagger \sigma_{01}, \quad (10)
$$

$$
\dot{a} = -[(\kappa_l + \kappa_r)/2 - i(\delta_p - \delta_c)]a - ig_1^* N\sigma_{01}
$$
$$
- ig_2^* N\sigma_{02} + \sqrt{\kappa_l/\tau}a_{\text{in}}^l + \sqrt{\kappa_r/\tau}a_{\text{in}}^r, \quad (11)
$$

where we replace all the operators with their average values but use the same notations for brevity.

Following the approach of Refs. [12,74], we consider the situations $\gamma_1 = \gamma_2 = \gamma$ and $g_1 = g_2 = g$ (g takes a real number). $g_1\sqrt{N} = g_2\sqrt{N} = g\sqrt{N}$ is the collective cavity-atom coupling strength for N atoms [i.e., the collective cavity-atom coupling strengths to two transition paths are identical; see Fig. 1(b)] [47,48,74,80]. The cavity can be treated as symmetric (i.e., $T_l = T_r = T$) so that $\kappa_l = \kappa_r = \kappa$ [12,47,48]. Also, we assume that the atomic system is closed, i.e., $\sigma_{00} + \sigma_{11} + \sigma_{22} = 1$ [12]. Under the steady-state condition, the left sides of Eqs. (5)–(11) [i.e., $\dot{\sigma}_{lm}$ $(l, m = 0, 1, 2)$ and $\dot{a}$] are set to zero. Then, by solving the corresponding algebraic equations, we can derive the steady-state solution of the intracavity light field a, yielding

$$
a = \frac{\sqrt{\kappa/\tau}(a_{\text{in}}^l + a_{\text{in}}^r)}{\kappa - i(\delta_p - \delta_c) + igN(\sigma_{01}' + \sigma_{02}')}, \quad (12)
$$

with $\sigma_{01}' = \sigma_{01}/a$ and $\sigma_{02}' = \sigma_{02}/a$. Under the steady-state condition, $\sigma_{01} = \sigma_{01}'a$ and $\sigma_{02} = \sigma_{02}'a$ can be obtained by solving Eqs. (5)–(11), where σ_{01}' and σ_{02}' are the formal coefficients composed of the system parameters and can be determined as in the following discussions.

The output light fields from the left and right mirrors of the cavity can be derived from the following input-output relations [10,12,46–48,64]:

$$
a_{\text{out}}^l = \sqrt{T}a - a_{\text{in}}^l, \quad (13)
$$

$$
a_{\text{out}}^r = \sqrt{T}a - a_{\text{in}}^r. \quad (14)
$$

Combining Eqs. (12)–(14), the steady-state solutions of the output light fields from the left and right mirrors of the CQED system are

$$
a_{\text{out}}^l = \frac{\kappa(a_{\text{in}}^l + a_{\text{in}}^r)}{\kappa - i(\delta_p - \delta_c) + igN(\sigma_{01}' + \sigma_{02}')} - a_{\text{in}}^l \quad (15)
$$

and

$$
a_{\text{out}}^r = \frac{\kappa(a_{\text{in}}^l + a_{\text{in}}^r)}{\kappa - i(\delta_p - \delta_c) + igN(\sigma_{01}' + \sigma_{02}')} - a_{\text{in}}^r, \quad (16)
$$

respectively. We can assume the right input light field $a_{\text{in}}^r = |a_{\text{in}}^r|$, the left input light field $a_{\text{in}}^l = \alpha|a_{\text{in}}^r|e^{i\varphi}$ (α is a real number and φ is the relative phase between the two input light fields a_{in}^l and a_{in}^r), and the input-light intensity $|a_{\text{in}}|^2 = |a_{\text{in}}^r|^2$ [47]. The strength of the left (right) input light field in units of Hz is given by $\eta_p^l = \sqrt{\kappa/\tau}a_{\text{in}}^l$ ($\eta_p^r = \sqrt{\kappa/\tau}a_{\text{in}}^r$). The amplitude of the left (right) input light field in units of $\sqrt{\text{Hz}}$ is described by $E_p^l = \eta_p^l/\sqrt{\kappa} = a_{\text{in}}^l/\sqrt{\tau}$ ($E_p^r = \eta_p^r/\sqrt{\kappa} = a_{\text{in}}^r/\sqrt{\tau}$). Also, we can define the left (right) cavity-input power P_{in}^l (P_{in}^r) related to the amplitude by $P_{\text{in}}^l = \hbar\omega_c {E_p^l}^2$ ($P_{\text{in}}^r = \hbar\omega_c {E_p^r}^2$) [81–85]. Here, the expectation value of the number of photons is equal to the light intensity, that is to say, $|a|^2 = n$, $|a_{\text{in}}|^2 = n_{\text{in}}$, $|a_{\text{out}}^l|^2 = n_{\text{out}}^l$, and $|a_{\text{out}}^r|^2 = n_{\text{out}}^r$ [47]. Then, we can derive the left (right) cavity-input power $P_{\text{in}}^l = \hbar\omega_c \kappa \alpha^2 n_{\text{in}}/T$ ($P_{\text{in}}^r = \hbar\omega_c \kappa n_{\text{in}}/T$) [82,83]. Similarly, the left (right) cavity-output power is given by $P_{\text{out}}^l = \hbar\omega_c \kappa n_{\text{out}}^l/T$ ($P_{\text{out}}^r = \hbar\omega_c \kappa n_{\text{out}}^r/T$) and the cavity-inside (intracavity) power is described by $P_c = \hbar\omega_c \kappa n/T$. For the sake of simplicity, we can define the cavity-input power $P_{\text{in}} = P_{\text{in}}^r$ (i.e., $P_{\text{in}}^l = \alpha^2 P_{\text{in}}$). Finally, combining Eqs. (12), (15), and (16), the left and right cavity-output powers and the cavity-inside power related to the cavity-input power can be further expressed as

$$P_{\text{out}}^l = \left| \frac{\kappa(1 + \alpha e^{i\varphi})}{\kappa - i(\delta_p - \delta_c) + igN(\sigma_{01}' + \sigma_{02}')} - \alpha e^{i\varphi} \right|^2 P_{\text{in}}, \quad (17)$$

$$P_{\text{out}}^r = \left| \frac{\kappa(1 + \alpha e^{i\varphi})}{\kappa - i(\delta_p - \delta_c) + igN(\sigma_{01}' + \sigma_{02}')} - 1 \right|^2 P_{\text{in}}, \quad (18)$$

$$P_c = \left| \frac{\kappa(1 + \alpha e^{i\varphi})}{\kappa - i(\delta_p - \delta_c) + igN(\sigma_{01}' + \sigma_{02}')} \right|^2 P_{\text{in}}. \quad (19)$$

III. EXPERIMENTAL FEASIBILITY AND TYPICAL PARAMETERS FOR THE MODEL

Before proceeding, we briefly address the experimental feasibility of our scheme. In accordance with Ref. [74], we can employ the dipole-forbidden singlet to triplet optical transition $(5s^2)^1S_0$ to $(5s5p)^3P_1$ in an ensemble of ^{88}Sr (nuclear spin $I = 0$, no hyperfine structure, and wavelength 689 nm; see Refs. [86–90] for details) as a possible candidate for the CQED system. The excited state $(5s5p)^3P_1$ couples to the environment via spontaneous emission at the relatively slow decay rate of $\gamma = 2\pi \times 7.5$ kHz. In ^{88}Sr, the nuclear spin $I = 0$ [74,87] means that the $(5s^2)^1S_0$ ground state is unique [the electronic angular momentum of the $(5s^2)^1S_0$ ground state is $J = 0$, and the hyperfine state $F = I + J = 0$ [87], i.e., the $(5s^2)^1S_0$ ground state does not split], while the $(5s5p)^3P_1$ excited state has two bright excited Zeeman sublevels. Therefore, the designated three-level V-type atomic states can be chosen as follows: $|0\rangle = |^1S_0\rangle$, $|1\rangle = |^3P_1, m_F = -1\rangle$, and $|2\rangle = |^3P_1, m_F = 1\rangle$, where m_F denotes the Zeeman substate [see Fig. 1(b); the $|^3P_1, m_F = 0\rangle$ is the dark state and does not interact with the horizontally polarized cavity mode].

By applying a Faraday magnetic field B directed along the z axis, a Zeeman splitting Δ_B can be generated between the bright excited states $|1\rangle$ and $|2\rangle$; see Fig. 1(b). According to Ref. [74], Δ_B is described by $\Delta_B/2\pi = g_e\mu_B B = B(2.1$ MHz/G), where $g_e = 1.5$ is the Landé g factor of the $(5s5p)^3P_1$ excited state [86,91], $\mu_B = 57.9$ μeV/T is the Bohr magneton [92], and G is Gauss with 1 G $= 10^{-4}$ T. In order to fit the magnitude of the magnetic field ($\sim$μT) used in this paper and the simplicity of the following formula, the Zeeman splitting Δ_B can also be expressed as $\Delta_B = g_B B = B(2\pi \times 21$ kHz/μT). $g_B = 2\pi \times 21$ kHz/μT is just a notation related to the Landé g factor and the Bohr magneton. As in experimental report [74], the strengths of the Faraday magnetic field used in this paper can be reached. The magnetic field introduced in our scheme can be continuously varied (or scanned) *in situ* by applying a voltage scan generator connected to the current source, like in Ref. [93].

A strongly coupled CQED system can be created by loading $N \approx 10^5$ ^{88}Sr atoms (the peak trap depth can reach $\approx$100 μK and the atoms can be cooled by laser to $\approx$10 μK) into a high-finesse two-sided optical Fabry-Pérot cavity [74,88–90]. The ensemble is dilute like in Refs. [74,80], so direct or (dipole-dipole) interaction between the atoms can be ignored. The resonance frequency ω_c of the cavity mode can be modulated to be near resonance with the transition frequency ω_0 of the dipole-forbidden singlet to triplet optical transition $^1S_0$ to $^3P_1$, that is, $\omega_c = \omega_0 = 2\pi c/\lambda$ (c is the speed of light and λ is 689 nm). The linewidth κ of the Fabry-Pérot cavity (the decay rate of the cavity mode) used in this paper is comparable to the decay rate γ of the atoms, which is realized in Refs. [94–98]. For example, the cavity with the linewidth is $\kappa = 2\pi \times 7.5$ kHz, the length is $L = 58.1$ mm [99], and the finesse (roughly the number of intracavity photon round trips during the cavity decay time) is $F = \pi c/(\kappa L) = 3.44 \times 10^5$ [100]. Also, the cavity with smaller length and higher fineness is realized in Refs. [101,102]. The collective cavity-atom coupling strength $g\sqrt{N}$ selected in this paper is also easy to implement in experiment [74]. Specifically, the typical collective cavity-atom coupling strength $g\sqrt{N} = 10\gamma = 2\pi \times 75$ kHz (and $g\sqrt{N} = 15\gamma = 2\pi \times 112.5$ kHz) is within a reasonable range of experimental parameters [88,90]. The parameter conditions for the implementation of our scheme are available.

IV. TUNABLE CPA AND CPT IN THE LINEAR EXCITATION REGIME

Assuming that the cavity-input power P_{in} is weak, the atomic populations are predominantly concentrated in the ground state $|0\rangle$ [$\sigma_{00} \approx 1$, $\sigma_{11} \approx 0$, and $\sigma_{22} \approx 0$, i.e., Holstein-Primakoff-approximation [103]; see Fig. 1(b)]. The CQED system is in the linear excitation regime [12,46,48]. By solving Eqs. (5)–(11), the steady-state solution of the intracavity light field a can be simplified as

$$a = \frac{\sqrt{\kappa/\tau}(a_{\text{in}}^l + a_{\text{in}}^r)}{\kappa - i(\delta_p - \delta_c) + \frac{g^2N(\gamma - 2i\delta_p)}{[\gamma/2 - i(\delta_p + g_B B/2)][\gamma/2 - i(\delta_p - g_B B/2)]}}, \quad (20)$$

where $\sigma_{01}' = \frac{-ig}{\gamma/2 - i(\delta_p + g_B B/2)}$ and $\sigma_{02}' = \frac{-ig}{\gamma/2 - i(\delta_p - g_B B/2)}$ [see Eq. (12)].

From Eqs. (17)–(19), the left and right cavity-output powers and the cavity-inside power related to the cavity-input power in the linear excitation regime of the CQED system can be, respectively, written as

$$P_{\text{out}}^l = \left| \frac{\kappa(1 + \alpha e^{i\varphi})}{\kappa - i(\delta_p - \delta_c) + \frac{g^2 N(\gamma - 2i\delta_p)}{[\gamma/2 - i(\delta_p + g_B B/2)][\gamma/2 - i(\delta_p - g_B B/2)]}} - \alpha e^{i\varphi} \right|^2 P_{\text{in}},$$ (21)

$$P_{\text{out}}^r = \left| \frac{\kappa(1 + \alpha e^{i\varphi})}{\kappa - i(\delta_p - \delta_c) + \frac{g^2 N(\gamma - 2i\delta_p)}{[\gamma/2 - i(\delta_p + g_B B/2)][\gamma/2 - i(\delta_p - g_B B/2)]}} - 1 \right|^2 P_{\text{in}},$$ (22)

$$P_c = \left| \frac{\kappa(1 + \alpha e^{i\varphi})}{\kappa - i(\delta_p - \delta_c) + \frac{g^2 N(\gamma - 2i\delta_p)}{[\gamma/2 - i(\delta_p + g_B B/2)][\gamma/2 - i(\delta_p - g_B B/2)]}} \right|^2 P_{\text{in}}.$$ (23)

If the two input light fields are identical, $a_{\text{in}}^l = a_{\text{in}}^r$ ($\alpha = 1$ and $\varphi = 0$), i.e., $P_{\text{in}}^l = P_{\text{in}}^r = P_{\text{in}}$, and it is easy to find that the left and right cavity-output powers are equal, $P_{\text{out}}^l = P_{\text{out}}^r = P_{\text{out}}$. First the CPA can occur in the CQED system when the magnetic field is present, in which the two cavity-output powers are zero ($P_{\text{out}}^l = P_{\text{out}}^r = P_{\text{out}} = 0$). Combining Eq. (21) with Eq. (22), we can derive the two specific parameter matching conditions for the CPA in the CQED system as follows:

$$\kappa\gamma\delta_p = (\delta_p - \delta_c)\left\{ \frac{[\gamma^2 + (g_B B)^2]}{4} - \delta_p^2 \right\} + 2g^2 N \delta_p$$ (24)

and

$$\gamma\delta_p(\delta_p - \delta_c) = -\kappa\left\{ \frac{[\gamma^2 + (g_B B)^2]}{4} - \delta_p^2 \right\} + g^2 N\gamma.$$ (25)

When Eqs. (24) and (25) are satisfied, there is no output light transmitted from the CQED system (i.e., the cavity-output power P_{out} is null), but the cavity-inside power P_c is not zero. That is to say, the two input light fields can be absorbed and then dissipated in the CQED system, which means that the CQED system can act as a perfect photon absorber.

In particular, the CPA can occur in the CQED system when the magnetic field is off ($B = 0$), in which the two cavity-output powers are zero ($P_{\text{out}}^l = P_{\text{out}}^r = P_{\text{out}} = 0$). Similarly, combining Eq. (21) with Eq. (22), we can derive the two specific parameter matching conditions for the CPA in the CQED system as follows:

$$\frac{\delta_p - \delta_c}{\delta_p} = \frac{2\kappa}{\gamma}$$ (26)

and

$$\delta_p(\delta_p - \delta_c) = 2g^2 N - \frac{\kappa\gamma}{2}.$$ (27)

Figure 2 provides a physical picture of the cavity MIT control of both CPA and CPT in the CQED system. Since the two orthogonal components of the input light fields can couple the two distinct Zeeman sublevels [the excited states $|1\rangle$ and $|2\rangle$; see Fig. 2(a)], the coupled CQED system has three polarization states [see Fig. 2(b)], with the form

$$|\Psi_+\rangle = \frac{1}{\sqrt{N_+}}\left[|c\rangle|0_c\rangle + \frac{x_1 - x_2}{g^2 N}|b\rangle|0_c\rangle - \frac{y_1 - y_2}{g\sqrt{N}}|a\rangle|1_c\rangle \right],$$ (28)

$$|\Psi_d\rangle = \frac{1}{\sqrt{N_d}}\left[|c\rangle|0_c\rangle - |b\rangle|0_c\rangle - \frac{y_1}{g\sqrt{N}}|a\rangle|1_c\rangle \right],$$ (29)

$$|\Psi_-\rangle = \frac{1}{\sqrt{N_-}}\left[|c\rangle|0_c\rangle + \frac{x_1 + x_2}{g^2 N}|b\rangle|0_c\rangle - \frac{y_1 + y_2}{g\sqrt{N}}|a\rangle|1_c\rangle \right],$$ (30)

where $x_1 = g^2 N + (g_B B)^2/4$, $x_2 = \sqrt{(g_B B)^2/4 + 2g^2 N} \times (g_B B)/2$, $y_1 = (g_B B)/2$, and $y_2 = \sqrt{(g_B B)^2/4 + 2g^2 N}$, respectively. $N_+ = 1 + (x_1 - x_2)^2/g^4 N^2 + (y_1 - y_2)^2/g^2 N$, $N_d = 2 + y_1^2/g^2 N$, and $N_- = 1 + (x_1 + x_2)^2/g^4 N^2 + (y_1 + y_2)^2/g^2 N$ are the normalized coefficients. Here $|a\rangle$, $|b\rangle$, and $|c\rangle$ are the Dicke states [48] for the N atoms in the cavity
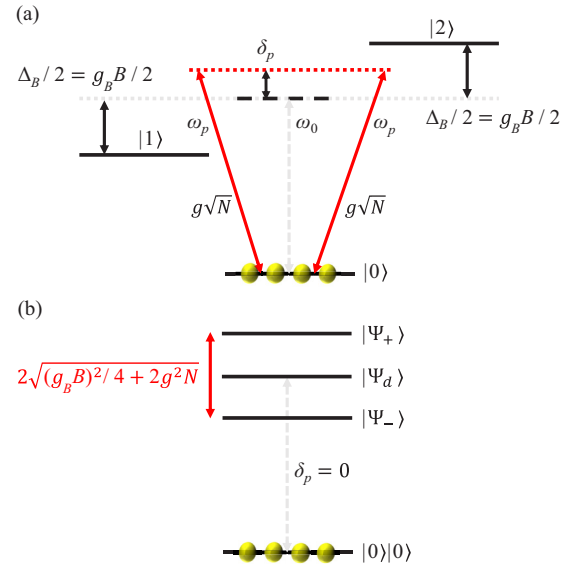

FIG. 2. (a) Energy-level structure of the three-level V-type atoms in the presence of an external magnetic field applied in the Faraday geometry. The Zeeman splitting Δ_B can be expressed as $\Delta_B = g_B B$ (see Sec. III above for details) and other symbols are consistent with the definitions in Fig. 1(b). (b) The corresponding polariton picture of the coupled CQED system with $\delta_c = 0$. Three polariton states are created: two bright polariton states $|\Psi_+\rangle$ and $|\Psi_-\rangle$, and a dark polariton state $|\Psi_d\rangle$. The frequency difference between the two bright polarization states is $2\sqrt{(g_B B)^2/4 + 2g^2 N}$. At $\delta_p = 0$, it excites the dark polariton state (cavity MIT) and leads to the CPA in the CQED system.
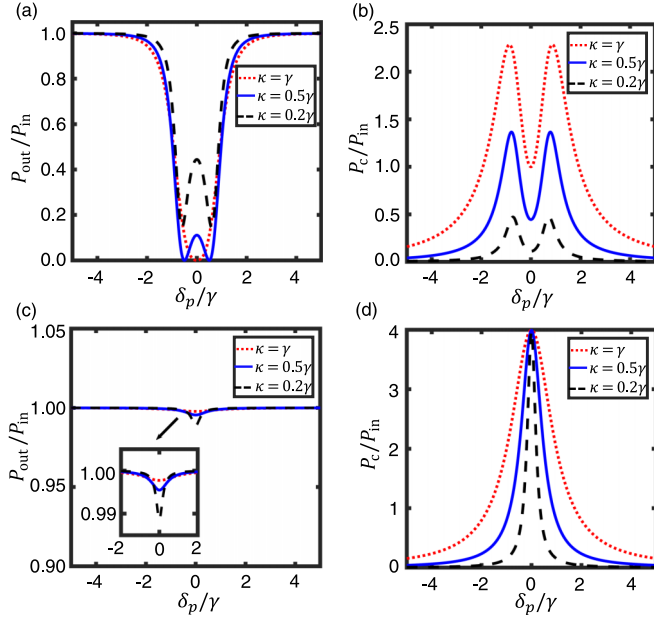
FIG. 3. (a) The normalized cavity-output power P_{out}/P_{in} ($P_{out}^l = P_{out}^r = P_{out}$) and (b) the corresponding normalized cavity-inside power P_c/P_{in} vs the input-light frequency detuning δ_p/γ with two identical input light fields $P_{in}^l = P_{in}^r = P_{in}$ when the magnetic field is off ($B = 0$). (c) The normalized cavity-output power P_{out}/P_{in} and (d) the corresponding normalized cavity-inside power P_c/P_{in} vs the input-light frequency detuning δ_p/γ when the magnetic field is present ($B = 15\ \mu$T). $\kappa = \gamma$ is denoted by the red-dotted line, $\kappa = 0.5\gamma$ is denoted by the blue-solid line, and $\kappa = 0.2\gamma$ is denoted by the black-dashed line. In panel (c), the inset shows the zoom-in region indicated by the arrow, which shares the same axis with panel (c). The other parameters are $g\sqrt{N} = 0.5\gamma$ (weak collective-coupling regime) and $\delta_c = 0$. The frequency parameters used in this paper are taken to have units of the atomic decay rate γ for simplicity and the specific parameters of the atoms are used according to the experimental data [74].

mode [$|a\rangle = |0, \ldots 0, \ldots 0\rangle$ (all N atoms are in the state $|0\rangle$), $|b\rangle = \frac{1}{\sqrt{N}} \sum_{i=1}^{N} |0, \ldots 1_i, \ldots 0\rangle$ (only one atom in the state $|1\rangle$), and $|c\rangle = \frac{1}{\sqrt{N}} \sum_{i=1}^{N} |0, \ldots 2_i, \ldots 0\rangle$ (only one atom in the state $|2\rangle$)]. $|0_c\rangle$ and $|1_c\rangle$ are zero-photon and one-photon states of the cavity mode. The frequency difference between the two bright polariton states $|\Psi_+\rangle$ and $|\Psi_-\rangle$ is $2\sqrt{(g_B B)^2/4 + 2g^2 N}$ as shown in Fig. 2(b). At $\delta_p = 0$, the dark polariton state $|\Psi_d\rangle$ leads to the CPA in the CQED system and is often referred to as cavity MIT [74].

In Fig. 3, we plot the normalized cavity-output power P_{out}/P_{in} and cavity-inside power P_c/P_{in} versus δ_p/γ when the magnetic field is absent [$B = 0$; see Figs. 3(a) and 3(b)] or present [$B = 15\ \mu$T; see Figs. 3(c) and 3(d)] under the weak collective-coupling regime of $g^2 N \ll \kappa\gamma$. The cavity mode and the atoms are on resonance, that is, $\omega_c = \omega_0$ (i.e., $\delta_c = 0$). Without the magnetic field, the input light fields can be completely absorbed at $\delta_p = 0$ for $\kappa = \gamma$ (the red-dotted line) and absorbed at $\delta_p = \pm\sqrt{2g^2 N - \kappa\gamma/2} = \pm 0.5\gamma$ for $\kappa = 0.5\gamma$ (the blue-solid line) with $g\sqrt{N} = 0.5\gamma$, as shown in Fig. 3(a). It is obvious from Fig. 3(a) that the occurrence of the CPA needs to satisfy the parameter matching conditions,

i.e., Eqs. (26) and (27). The CPA is sensitive to the system parameters κ, γ, δ_p, and $g\sqrt{N}$. We can insert the Hamiltonian of Eq. (3) and the system wave function into the Schrödinger equation like in Ref. [12] and derive that the two peaks in Fig. 3(b) are located at $\delta_p = \pm\sqrt{2g^2 N}$. The corresponding normalized cavity-inside power P_c/P_{in} is not zero and has two peaks, which means that the photon energy of the input light fields is converted into internal excitation energy at two bright polariton excitations of the system [12,48]. When the magnetic field is present ($B = 15\ \mu$T), the points of the CPA in Fig. 3(a) become nearly CPT, which is caused by the large detuning between the state $|1\rangle$ and the state $|2\rangle$ from the cavity induced by the Zeeman splitting, as shown in Fig. 3(c). The existence of the magnetic field can result in an even greater intracavity light field [see Fig. 3(d)].

Under the strong collective-coupling regime of $g^2 N \gg \kappa\gamma$ and the parameter matching conditions of the CPA [12,46,48], Figs. 4(a) and 4(b) show the normalized cavity-output power P_{out}/P_{in} and the corresponding normalized cavity-inside power P_c/P_{in} versus the input-light frequency detuning δ_p/γ when the magnetic field is off ($B = 0$). At the two polariton resonances $\delta_p = \pm\sqrt{2g^2 N}$ [points Z and X with $\delta_p = \pm 21.21\gamma$ and points F and E with $\delta_p = \pm 14.14\gamma$] [12,48], $P_{out}^l = P_{out}^r = P_{out} = 0$, but P_c/P_{in} is located at the peaks [see Fig. 4(b)], indicating that the CQED system can act as a perfect photon absorber. Figures 4(c) and 4(d) show the normalized cavity-output power P_{out}/P_{in} and the corresponding normalized cavity-inside power P_c/P_{in} versus the input-light frequency detuning δ_p/γ when the magnetic field is present ($B = 15\ \mu$T). In Fig. 4(c), the CPA can occur at $\delta_p = 0$ (point Y') with $g\sqrt{N} = 15\gamma$ (the blue-solid line), which satisfies the parameter matching conditions [i.e., Eqs. (24) and (25)]. Compared with the case without applying the magnetic field in Fig. 4(a) (point Y for the blue-solid line; the normalized cavity-output power is $P_{out}/P_{in} = 1$, the input light fields can be completely transmitted, and the CPT occurs), the existence of the magnetic field can realize the conversion of the CQED system from a perfect photon absorber to a perfect photon transmitter. The points at $\delta_p = \pm 21.21\gamma$ (points X and Z) for the blue-solid line and at $\delta_p = \pm 14.14\gamma$ (points E and F) for the red-dotted line of the CPA in Fig. 4(a) without the magnetic field become completely transmitted (points X', Z', E', and F') after the magnetic field is applied as shown in Fig. 4(c). By simply turning the magnetic field on or off, the CQED system can act as a perfect absorber or perfect transmitter at multiple input light frequencies instead of only one single frequency, which relaxes the frequency requirements in the scheme based on the EIT configuration [48]. The two sideband dips in Fig. 4(c) and two sideband peaks in Fig. 4(d) are located at $\delta_p = \pm\sqrt{(g_B B)^2/4 + 2g^2 N}$ [12] ($\delta_p = \pm 29.85\gamma$ for the blue-solid line and $\delta_p = \pm 25.32\gamma$ for the red-dotted line; see Sec. III for the specific parameters). For the blue-solid line at $\delta_p = 0$ (point Y'), the normalized cavity-output power is $P_{out}/P_{in} = 0$ [see Fig. 4(c)] and the corresponding normalized cavity-inside power is $P_c/P_{in} = 1$ [see Fig. 4(d)], indicating that no light can be transmitted from the cavity and the input light fields are almost completely absorbed by the cavity mirrors.

The underlying physical mechanism of the CPA can be better understood and described by presenting the results for
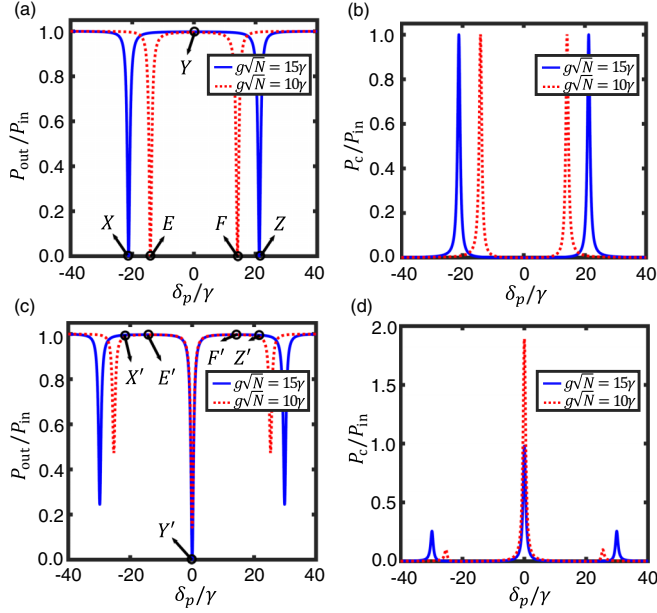
FIG. 4. (a) The normalized cavity-output power $P_{\text{out}}/P_{\text{in}}$ and (b) the corresponding normalized cavity-inside power P_c/P_{in} vs the input-light frequency detuning δ_p/γ when the magnetic field is off ($B = 0$). (c) The normalized cavity-output power $P_{\text{out}}/P_{\text{in}}$ and (d) the corresponding normalized cavity-inside power P_c/P_{in} vs the input-light frequency detuning δ_p/γ when the magnetic field is present ($B = 15$ μT). $g\sqrt{N} = 15\gamma$ (strong collective-coupling regime) is denoted by the blue-solid line and $g\sqrt{N} = 10\gamma$ (strong collective-coupling regime) is denoted by the red-dotted line. The three points of X ($P_{\text{out}}/P_{\text{in}} = 0$), Y ($P_{\text{out}}/P_{\text{in}} = 1$), and Z ($P_{\text{out}}/P_{\text{in}} = 0$) in panel (a), respectively, represent the normalized cavity-output power $P_{\text{out}}/P_{\text{in}}$ of $\delta_p = -21.21\gamma$, 0, and $+21.21\gamma$ for $g\sqrt{N} = 15\gamma$ (the blue-solid line) when the magnetic field is off ($B = 0$), and the three points of X' ($P_{\text{out}}/P_{\text{in}} = 1$), Y' ($P_{\text{out}}/P_{\text{in}} = 0$), and Z' ($P_{\text{out}}/P_{\text{in}} = 1$) in panel (c) correspond to the case when the magnetic field is present ($B = 15$ μT), respectively. The two points of E ($P_{\text{out}}/P_{\text{in}} = 0$) and F ($P_{\text{out}}/P_{\text{in}} = 0$) in panel (a), respectively, represent the normalized cavity-output power $P_{\text{out}}/P_{\text{in}}$ of $\delta_p = -14.14\gamma$ and $+14.14\gamma$ for $g\sqrt{N} = 10\gamma$ (the red-dotted line) when the magnetic field is off ($B = 0$), and the two points of E' ($P_{\text{out}}/P_{\text{in}} = 1$) and F' ($P_{\text{out}}/P_{\text{in}} = 1$) in panel (c) correspond to the case when the magnetic field is present ($B = 15$ μT), respectively. The other parameters are $P_{\text{in}}^l = P_{\text{in}}^r = P_{\text{in}}$, $P_{\text{out}}^l = P_{\text{out}}^r = P_{\text{out}}$, $\kappa = 0.5\gamma$, and $\delta_c = 0$.

intermediate values of the magnetic field in Fig. 4(c). When the magnetic field approaches zero [the orange-dotted line; see Fig. 5], the two bright polariton states $|\Psi_+\rangle$ and $|\Psi_-\rangle$ at $\pm\sqrt{2g^2N}$ ($\pm 21.21\gamma$) lead to the transmission dips. There is also a third dark polariton state $|\Psi_d\rangle$, the frequency of which is equal to that of the atomic transition [see Fig. 2(b)]. According to Eq. (29), as the magnetic field approaches zero, $y_1 = (g_B B)/2$ approaches zero, and the dark polariton state can be composed of an equal superposition of the two Zeeman sublevels [i.e., $|\Psi_d\rangle = \frac{1}{\sqrt{N_d}}(|c\rangle|0_c\rangle - |b\rangle|0_c\rangle)$]. The dark polariton state $|\Psi_d\rangle$ is entirely atomlike and the photonlike component ($|a\rangle|1_c\rangle$) vanishes as the magnetic field approaches zero [74], so the orange-dotted line in Fig. 5 has no transmission dip at $\delta_p = 0$. When a magnetic field is applied perpendicular to the polarizations of the input light fields, the
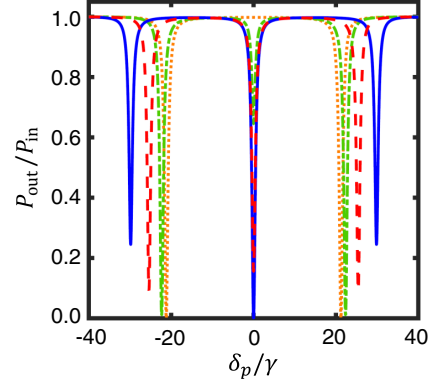

FIG. 5. The normalized cavity-output power $P_{\text{out}}/P_{\text{in}}$ vs the input-light frequency detuning δ_p/γ with $g\sqrt{N} = 15\gamma$. Each kind of line is obtained under different applied magnetic fields. $B = 0$ μT is denoted by the orange-dotted line, $B = 5$ μT is denoted by the green-dash-dotted line, $B = 10$ μT is denoted by the red-dashed line, and $B = 15$ μT is denoted by the blue-solid line. The other parameters are $P_{\text{in}}^l = P_{\text{in}}^r = P_{\text{in}}$, $P_{\text{out}}^l = P_{\text{out}}^r = P_{\text{out}}$, $\kappa = 0.5\gamma$, and $\delta_c = 0$.

photonic character $|a\rangle|1_c\rangle$ can be mixed into the dark polariton state [i.e., Eq. (29)], inducing a new transmission feature between the two original resonances of the vacuum Rabi splitting. As shown in Fig. 5, a new transmission dip appears (the green-dash-dotted line, the red-dashed line, and the blue-solid line) at $\delta_p = 0$, and the CPA occurs (the blue-solid line) when the parameter matching conditions [i.e., Eqs. (24) and (25)] are satisfied. In order to study how the CPA performance of the CQED system varies versus the collective cavity-atom coupling strength $g\sqrt{N}$, we plot the normalized cavity-output power $P_{\text{out}}/P_{\text{in}}$ in Fig. 6(a) and the corresponding normalized cavity-inside power P_c/P_{in} in Fig. 6(b) versus $g\sqrt{N}/\gamma$ when the magnetic field is off ($B = 0$). It can be seen from Figs. 6(a) and 6(b), under the strong collective-coupling regime of $g^2N \gg \kappa\gamma$, that the input light fields can be completely coupled into the cavity mode ($P_c/P_{\text{in}} = 1$) and there is no output light field ($P_{\text{out}}/P_{\text{in}} = 0$), indicating that the CQED system can act as a perfect photon absorber. Compared with the previous work [48] in which the CPA is induced by an external control light field, under $g\sqrt{N} < 5\gamma$, we show that the proposed CPA scheme has better absorption (i.e., the normalized cavity-output power $P_{\text{out}}/P_{\text{in}}$ tends to zero) than the reported result in the previous work [48]. Figures 6(c) and 6(d) show the normalized cavity-output power $P_{\text{out}}/P_{\text{in}}$ and the corresponding normalized cavity-inside power P_c/P_{in} versus $g\sqrt{N}/\gamma$ when the magnetic field is present ($B = 15$ μT is denoted by the black-dashed line, $B = 10$ μT is denoted by the blue-solid line, and $B = 5$ μT is denoted by the red-dotted line). As can be seen from Figs. 6(a) and 6(c), the magnetic field can be used as a switch between photon absorption [$P_{\text{out}}/P_{\text{in}} = 0$; see Fig. 6(a)] and photon transmission [$P_{\text{out}}/P_{\text{in}} = 1$ is denoted by the black-dashed line; see Fig. 6(c)]. With the increase of the magnetic field B, the robustness of the normalized cavity-output power to the collective cavity-atom coupling strength $g\sqrt{N}$ increases and the value of the normalized cavity-output power tends to unity, but the corresponding normalized cavity-inside power is maintained to be near zero, which
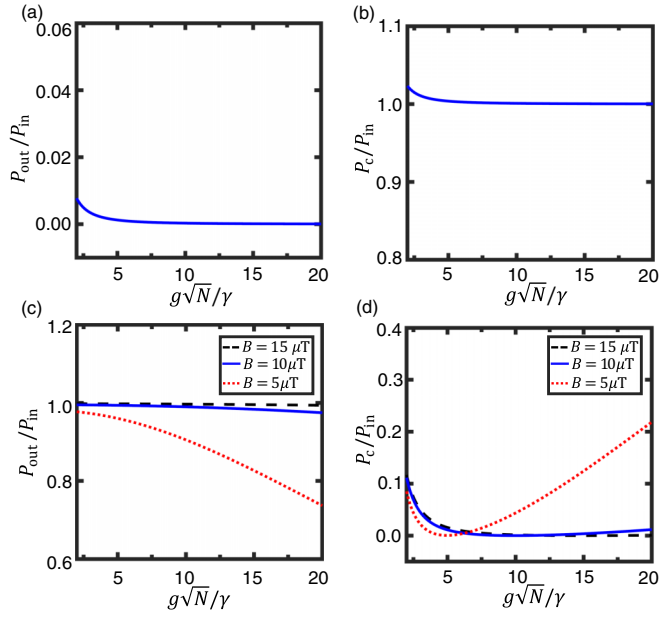
FIG. 6. (a) The normalized cavity-output power P_{out}/P_{in} and (b) the corresponding normalized cavity-inside power P_c/P_{in} vs the collective cavity-atom coupling strength $g\sqrt{N}/\gamma$ when the magnetic field is off ($B = 0$). (c) The normalized cavity-output power P_{out}/P_{in} and (d) the corresponding normalized cavity-inside power P_c/P_{in} vs the collective cavity-atom coupling strength $g\sqrt{N}/\gamma$ when the magnetic field is present ($B = 15\,\mu$T is denoted by the black-dashed line, $B = 10\,\mu$T is denoted by the blue-solid line, and $B = 5\,\mu$T is denoted by the red-dotted line). The other parameters are $P_{in}^l = P_{in}^r = P_{in}$, $P_{out}^l = P_{out}^r = P_{out}$, $\kappa = 0.5\gamma$, $\delta_p = \sqrt{2g^2N}$, and $\delta_c = 0$.

means that the transmission characteristics of the CQED system depend on the magnetic field B.

Figures 7(a) and 7(b) plot the normalized cavity-output power P_{out}/P_{in} and the corresponding normalized cavity-inside power P_c/P_{in} versus the magnetic field B. As can be seen from the inset in Fig. 7(a), the CPA is robust to the variation of the magnetic field when the magnetic-field strength is near zero (the range of the variation is $-0.6 < B < 0.6\,\mu$T),
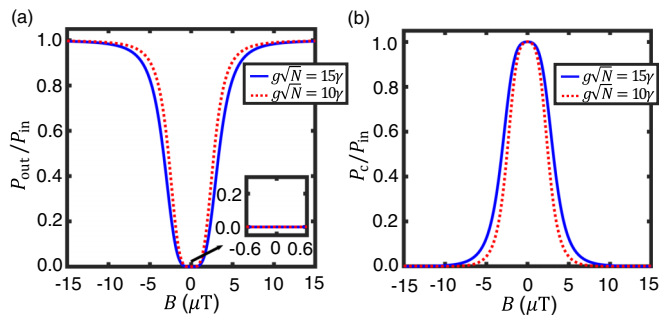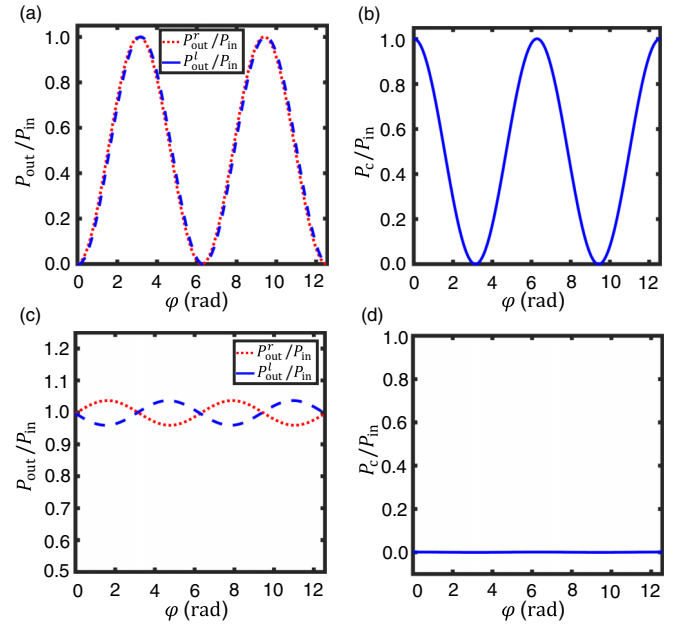

FIG. 7. (a) The normalized cavity-output power P_{out}/P_{in} and (b) the corresponding normalized cavity-inside power P_c/P_{in} vs the magnetic field B. $g\sqrt{N} = 15\gamma$ is denoted by the blue-solid line and $g\sqrt{N} = 10\gamma$ is denoted by the red-dotted line. In panel (a), the inset shows the zoom-in region indicated by the arrow, which shares the same axis with panel (a). The other parameters are $P_{in}^l = P_{in}^r = P_{in}$, $P_{out}^l = P_{out}^r = P_{out}$, $\kappa = 0.5\gamma$, $\delta_p = \sqrt{2g^2N}$, and $\delta_c = 0$.

FIG. 8. (a) The normalized cavity-output power P_{out}/P_{in} and (b) the corresponding normalized cavity-inside power P_c/P_{in} vs the relative phase φ between the two input light fields $a_{in}^r = |a_{in}^r|$ and $a_{in}^l = \alpha|a_{in}^r|e^{i\varphi}$ when the magnetic field is off ($B = 0$). (c) The normalized cavity-output power P_{out}/P_{in} and (d) the corresponding normalized cavity-inside power P_c/P_{in} vs the relative phase φ between the two input light fields when the magnetic field is present ($B = 15\,\mu$T). In panels (a) and (c), the normalized right cavity-output power P_{out}^r/P_{in} is denoted by the red-dotted line and the normalized left cavity-output power P_{out}^l/P_{in} is denoted by the blue-dashed line. The other parameters are $P_{in}^l = P_{in}^r = P_{in}$, $g\sqrt{N} = 10\gamma$, $\kappa = 0.5\gamma$, $\delta_p = \sqrt{2g^2N}$, and $\delta_c = 0$.

while the input light fields can be almost completely coupled into the cavity mode [see Fig. 7(b)]. With the increase of the collective cavity-atom coupling strength $g\sqrt{N}$, the range can be broadened slightly. With the increase of the magnetic field, the input light fields are basically transmitted from the CQED system, and no light can be coupled into the cavity mode. By adjusting the magnetic field properly, the CQED system can be converted from a perfect photon absorber (no cavity-output power but with a large cavity-inside power) into a nearly perfect photon transmitter (nearly perfect transmission for the input light fields and no cavity-inside power).

According to Eqs. (21) and (22), the CPA in the CQED system can also be controlled by varying the relative phase φ between the two input light fields $a_{in}^r = |a_{in}^r|$ and $a_{in}^l = \alpha|a_{in}^r|e^{i\varphi}$. Figures 8(a) and 8(b) show the normalized cavity-output power P_{out}/P_{in} and the corresponding normalized cavity-inside power P_c/P_{in} versus the relative phase φ when the magnetic field is off ($B = 0$). When $\varphi = 2n\pi$ (n takes an integer), the normalized right cavity-output power P_{out}^r/P_{in} (the red-dotted line) and the normalized left cavity-output power P_{out}^l/P_{in} (the blue-dashed line) are equal to zero. Correspondingly, the normalized cavity-inside power P_c/P_{in} is equal to a value of 1. When $\varphi = (2n + 1)\pi$, the CQED system displays an opposite behavior, that is to say, the normalized right cavity-output power P_{out}^r/P_{in} (the red-dotted
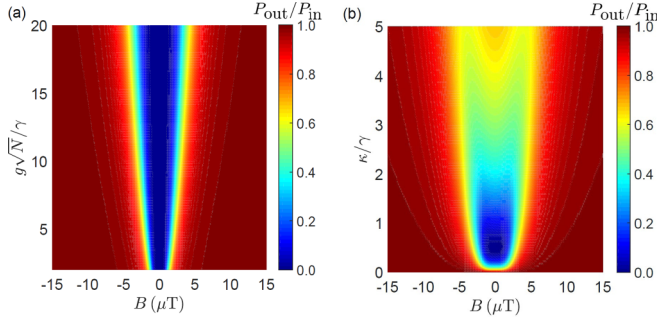
FIG. 9. (a) Contour plot of the normalized cavity-output power P_{out}/P_{in} as a function of the magnetic field B as well as the collective cavity-atom coupling strength $g\sqrt{N}/\gamma$ with $\kappa = 0.5\gamma$. (b) Contour plot of the normalized cavity-output power P_{out}/P_{in} as a function of the magnetic field B as well as the cavity decay rate κ/γ with $g\sqrt{N} = 10\gamma$. The other parameters are $P_{in}^l = P_{in}^r = P_{in}$, $P_{out}^l = P_{out}^r = P_{out}$, $\delta_p = \sqrt{2g^2N}$, and $\delta_c = 0$.

line) and the normalized left cavity-output power P_{out}^l/P_{in} (the blue-dashed line) are equal to unity, while the corresponding normalized cavity-inside power P_c/P_{in} is equal to a zero value. Figures 8(c) and 8(d) show the normalized cavity-output power P_{out}/P_{in} and the corresponding normalized cavity-inside power P_c/P_{in} versus the relative phase φ when the magnetic field is present ($B = 15$ μT). When $\varphi = n\pi$, the normalized right cavity-output power P_{out}^r/P_{in} (the red-dotted line) and the normalized left cavity-output power P_{out}^l/P_{in} (the blue-dashed line) are equal to unity and no light can be coupled into the cavity. When $\varphi = 2n\pi$ (i.e., the two input light fields are the same), the CQED system can realize the conversion between the CPA and CPT by simply turning the magnetic field on or off. Different from Ref. [12], the scheme based on the MIT configuration can realize the conversion between the CPA and CPT without the need for changing the optical characteristics (i.e., the phase) of the absorbed lights. The introduction of the magnetic field can relax the requirement for the absorbed lights.

On the basis of analysis so far, in order to more clearly show the influence of the system parameters on the transmission characteristics of the CQED system, we plot

the two-dimensional map of the normalized cavity-output power P_{out}/P_{in} as a function of the magnetic field B as well as the collective cavity-atom coupling strength $g\sqrt{N}/\gamma$ with $\kappa = 0.5\gamma$ in Fig. 9(a). It can be clearly seen from Fig. 9(a) that the CPA window can occur in a small range where the magnetic field $B = 0$, and the CPT can appear with the increase of the magnetic field in the system. The CPA window can be broadened with the increase of the collective cavity-atom coupling strength $g\sqrt{N}$, which is consistent with that shown in Fig. 7(a). Figure 9(b) shows the normalized cavity-output power P_{out}/P_{in} as a function of the magnetic field B as well as the cavity decay rate κ/γ with $g\sqrt{N} = 10\gamma$. Under the strong collective-coupling regime and without the magnetic field, the CPA can occur at $\kappa = 0.5\gamma$, which satisfies the parameter matching conditions [i.e., Eqs. (26) and (27)].

Also, we plot the contour diagram showing the normalized right cavity-output power P_{out}^r/P_{in} in Fig. 10(a) and the normalized left cavity-output power P_{out}^l/P_{in} in Fig. 10(b) with respect to the magnetic field B as well as the relative phase φ between the two input light fields $a_{in}^r = |a_{in}^r|$ and $a_{in}^l = \alpha|a_{in}^r|e^{i\varphi}$. It is shown that the joint regulation of the magnetic field and the relative phase can better realize the conversion from the CPA to the CPT in the CQED system. Figure 10(c) shows the two-dimensional color-scale map of the normalized total cavity-output power P_{out}^t/P_{in} ($P_{out}^t = P_{out}^r + P_{out}^l$) as a function of the magnetic field B as well as the relative phase φ. It can be noted from Figs. 10(a) and 10(b) that the normalized cavity-output power (P_{out}^r/P_{in} or P_{out}^l/P_{in}) can be greater than 1, which is caused by the interference between the two input light fields under the applied magnetic field. Although the cavity-output power on one side of the cavity mirror can be greater than the cavity-input power ($P_{out}^r > P_{in}$ or $P_{out}^l > P_{in}$), the total cavity-output power is not greater than the total cavity-input power (the total cavity-output power is $2P_{in}$, i.e., the normalized total cavity-output power $P_{out}^t/P_{in} \leqslant 2$) as shown in Fig. 10(c). We can also see that under the appropriate relative phase φ the CPA can occur, and a nearly perfect photon absorption working window can appear near the magnetic field $B = 0$. The asymmetric input-output behavior [104,105] (i.e., the right and left cavity-output powers at both ends of the system are different from each
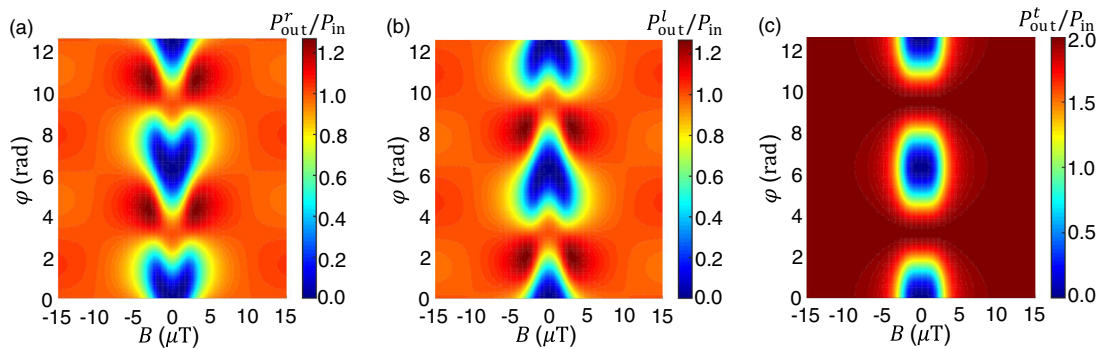

FIG. 10. (a) Contour plot of the normalized right cavity-output power P_{out}^r/P_{in} as a function of the magnetic field B as well as the relative phase φ between the two input light fields $a_{in}^r = |a_{in}^r|$ and $a_{in}^l = \alpha|a_{in}^r|e^{i\varphi}$. (b) Contour plot of the normalized left cavity-output power P_{out}^l/P_{in} as a function of the magnetic field B as well as the relative phase φ. (c) Contour plot of the normalized total cavity-output power P_{out}^t/P_{in} ($P_{out}^t = P_{out}^r + P_{out}^l$) as a function of the magnetic field B as well as the relative phase φ. The other parameters are $P_{in}^l = P_{in}^r = P_{in}$, $g\sqrt{N} = 10\gamma$, $\kappa = 0.5\gamma$, $\delta_p = \sqrt{2g^2N}$, and $\delta_c = 0$.

other) can be used for optical logic and optical communication devices [63,106].

V. TUNABLE CPA AND CPT IN THE NONLINEAR EXCITATION REGIME

When the cavity-input power P_{in} is strong enough, the atomic populations in the two excited states $|1\rangle$ and $|2\rangle$ are not equal to zero (i.e., $\sigma_{11} \neq 0$ and $\sigma_{22} \neq 0$) and Holstein-Primakoff-approximation therefore breaks down. In this case, the CQED system is in the nonlinear excitation regime [10,12,47,75]. By solving Eqs. (5)–(11), after lengthy algebra the steady-state solution of the intracavity light field a can be written as

$$a = \frac{\sqrt{\kappa/\tau}(a_{\text{in}}^l + a_{\text{in}}^r)}{\kappa - i(\delta_p - \delta_c) + \frac{4g^2N\{[(g_BB)^2 + (\gamma + 2i\delta_p)^2](\gamma - 2i\delta_p) + 8g^2|a|^2(\gamma + 2i\delta_p) + O(|a|^4)\}}{\{(g_BB)^4 + 2(g_BB)^2(\gamma^2 - 4\delta_p^2) + (\gamma^2 + 4\delta_p^2)^2 + 8g^2|a|^2[(g_BB)^2 + 3(\gamma^2 + 4\delta_p^2)] + O(|a|^4)\}}}. \quad (31)$$

Combining Eq. (17) with Eq. (18), we can derive the closed-form expressions of the left and right cavity-output powers nonlinearly related to the cavity-input power, with the forms

$$P_{\text{out}}^l = \left| \frac{\kappa(1 + \alpha e^{i\varphi})}{\kappa - i(\delta_p - \delta_c) + \frac{4g^2N\{[(g_BB)^2 + (\gamma + 2i\delta_p)^2](\gamma - 2i\delta_p) + 8g^2|a|^2(\gamma + 2i\delta_p) + O(|a|^4)\}}{\{(g_BB)^4 + 2(g_BB)^2(\gamma^2 - 4\delta_p^2) + (\gamma^2 + 4\delta_p^2)^2 + 8g^2|a|^2[(g_BB)^2 + 3(\gamma^2 + 4\delta_p^2)] + O(|a|^4)\}}} - \alpha e^{i\varphi} \right|^2 P_{\text{in}}, \quad (32)$$

$$P_{\text{out}}^r = \left| \frac{\kappa(1 + \alpha e^{i\varphi})}{\kappa - i(\delta_p - \delta_c) + \frac{4g^2N\{[(g_BB)^2 + (\gamma + 2i\delta_p)^2](\gamma - 2i\delta_p) + 8g^2|a|^2(\gamma + 2i\delta_p) + O(|a|^4)\}}{\{(g_BB)^4 + 2(g_BB)^2(\gamma^2 - 4\delta_p^2) + (\gamma^2 + 4\delta_p^2)^2 + 8g^2|a|^2[(g_BB)^2 + 3(\gamma^2 + 4\delta_p^2)] + O(|a|^4)\}}} - 1 \right|^2 P_{\text{in}}. \quad (33)$$

Although the higher-order items of a are neglected [i.e., $O(|a|^4)$; the results of ignoring $O(|a|^4)$ and those of not ignoring $O(|a|^4)$ will be compared later on], it is obvious that Eqs. (32) and (33) are the quadratic equations of a. Therefore, the closed-form formulas (32) and (33) show a nonlinear dependent relation between the cavity-output power and the cavity-input power. As expected, when the above $|a|^2$-dependent nonlinear terms are dropped, Eqs. (31)–(33) recover the linear results [see Eqs. (20)–(22)] in Sec. IV.

With two identical input light fields $P_{\text{in}}^l = P_{\text{in}}^r = P_{\text{in}}$ ($\alpha = 1$ and $\varphi = 0$), the cavity-input power and cavity frequency detuning under the condition of the CPA ($P_{\text{out}}^l = P_{\text{out}}^r = P_{\text{out}} = 0$) in the CQED system can be derived as

$$P_{\text{in}} = \frac{\hbar\omega_c\kappa\{4g^2N[\gamma^3 + \gamma(g_BB)^2 + 4\gamma\delta_p^2] - \kappa[(g_BB)^4 + 2(g_BB)^2(\gamma^2 - 4\delta_p^2) + (\gamma^2 + 4\delta_p^2)^2]\}}{8g^2\{\kappa[(g_BB)^2 + 3(\gamma^2 + 4\delta_p^2)] - 4g^2N\gamma\}} \quad (34)$$

and

$$\delta_c = \delta_p - \frac{4g^2N\{16g^2\delta_pP_{\text{in}} + \hbar\omega_c\kappa[2\gamma^2\delta_p - 2\delta_p(g_BB)^2 + 8\delta_p^3]\}}{8g^2P_{\text{in}}[(g_BB)^2 + 3(\gamma^2 + 4\delta_p^2)] + \hbar\omega_c\kappa[(g_BB)^4 + 2(g_BB)^2(\gamma^2 - 4\delta_p^2) + (\gamma^2 + 4\delta_p^2)^2]}. \quad (35)$$

It should be pointed out that with the increase of the cavity-input power, the nonlinear interaction between the cavity mode and the atoms becomes dominant in the CQED system [47]. In Fig. 11, we show the analytical results of the cavity-output power versus the cavity-input power for a series of different system parameters. The CPA is manifested by the destructive interference of the two input light fields of the scattered photons from the two excited states with opposite circular polarization under the Zeeman effect of the applied Faraday magnetic field and occurs at a given cavity-input power satisfying Eq. (34) with $\varphi = 2n\pi$ (the two input light fields are in phase and the two output light fields are equal; see the blue-dashed line in Fig. 11). When $\varphi = (2n + 1)\pi$, there is no light which can be coupled into the cavity mode and the two cavity-output powers P_{out}^r and P_{out}^l are equal to the cavity-input power P_{in} (see the black-solid line in Fig. 11). At other φ values, the two cavity-output powers P_{out}^r and P_{out}^l become generally different due to the interference of the two input light fields, and the CPA does not occur (see the red-dotted line and the purple-dash-dotted line for $\varphi = \pi/2$ in Fig. 11).

In the case of weak cavity-input power, for a given cavity-input power, there is only one real-value solution for P_{out}^r and P_{out}^l in Eqs. (32) and (33), and we can see that the nearly perfect photon absorption working window occurs [see the blue-dashed line in Figs. 11(a) and 11(b)]. However, with the increase of the cavity-input power, the nonlinear interaction between the cavity mode and the atoms dominates, and we can see that optical bistability occurs [see the blue-dashed line in Figs. 11(c) and 11(d)]. In the bistable domain, the closed-form formulas (32) and (33) have three real-value solutions for P_{out}^r and P_{out}^l corresponding to a given cavity-input power and the CPA point is near the turning point of the cavity-input power on the bistable return hysteresis curve. Under the condition of satisfying Eq. (34) and the control of the magnetic field, with the increase of the cavity-input power, the threshold (the lower one) of the bistability continues to increase as shown in Figs. 11(c) and 11(d). The CPA can occur
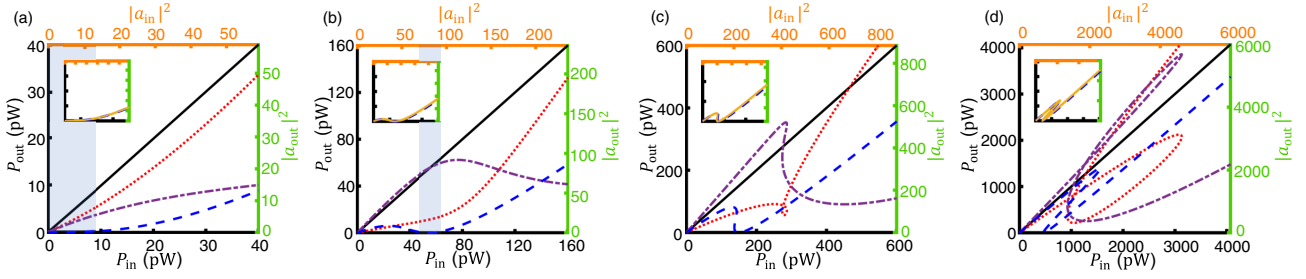
FIG. 11. The analytical results of the cavity-output power P_{out} (P_{out}^r or P_{out}^l) vs the cavity-input power P_{in} with two identical input light fields $P_{\text{in}}^l = P_{\text{in}}^r = P_{\text{in}}$, and varying the relative phase φ ($\varphi = \pi$ is denoted by the black-solid line for which the two cavity-output powers are equal, $P_{\text{out}}^l = P_{\text{out}}^r$; $\varphi = \pi/2$ is denoted by the red-dotted line and the purple-dash-dotted line for which the two cavity-output powers are different with the red-dotted line for the right cavity-output power P_{out}^r and the purple-dash-dotted line for the left cavity-output power P_{out}^l; $\varphi = 0$ is denoted by the blue-dashed line for which the two cavity-output powers are equal, $P_{\text{out}}^l = P_{\text{out}}^r$). These analytical results are calculated analytically using the closed-form formulas (32) and (33). The CPA can occur at $\varphi = 2n\pi$ ($n = 0, 1, 2, \ldots$, takes an integer). The top orange horizontal axis and the right green vertical axis show the input-light intensity $|a_{\text{in}}|^2$ and the output-light intensity $|a_{\text{out}}|^2$ in the CQED system, respectively. The shaded area in panels (a) and (b) indicates the nearly perfect photon absorption working window. In the case of $\varphi = 0$, the comparisons between the numerical results (the yellow-solid line, calculated numerically by the equations of motion of the CQED system) and the analytical results (the blue-dashed line, calculated analytically by the closed-form expressions) are shown in the insets, where the insets and the panels share the same axes. (a) $g\sqrt{N} = 10\gamma$, $\delta_c = 0$, and $B = 0$; (b) $g\sqrt{N} = 10\gamma$, $\delta_c = 0.59\gamma$, and $B = 1.5\ \mu\text{T}$; (c) $g\sqrt{N} = 12\gamma$, $\delta_c = 1.31\gamma$, and $B = 2.5\ \mu\text{T}$; (d) $g\sqrt{N} = 15\gamma$, $\delta_c = 3.09\gamma$, and $B = 4.5\ \mu\text{T}$. The other parameters are $\kappa = 0.5\gamma$, $g = 0.02\gamma$, $T = 0.01$, and $\delta_p = \sqrt{2g^2N}$.

at $P_{\text{in}} = 149.2$ pW with $B = 2.5\ \mu\text{T}$ [see Fig. 11(c)] and at $P_{\text{in}} = 468.2$ pW with $B = 4.5\ \mu\text{T}$ [see Fig. 11(d)]. Moreover, except for the bistable domain, the relationship between the cavity-input power and the cavity-output power in the CQED system is an approximate linear style (see the blue-dashed line). By the control of the magnetic field, our scheme can flexibly adjust the threshold of the CPA, which provides an optional scheme for adjustable bistability and a linear and magnetic-field controllable all-optical switching.

What is more, in the case of $\varphi = 0$, the numerical results (the yellow-solid line, calculated numerically; the higher-order items of a are not neglected) given by the equations of motion [i.e., Eqs. (5)–(11)] of the CQED system are compared with the analytical results (the blue-dashed line, calculated analytically; the higher-order items of a are neglected) given by the closed-form formulas (32) and (33) as displayed in the insets. It is revealed from the insets that the numerical results are in good agreement with those for the analytical calculations. In other words, the full numerical solutions achieved by the equations of motion of the CQED system can be perfectly reproduced by the closed-form formulas (32) and (33) obtained by ignoring the higher-order items of a.

In addition, Fig. 11 reveals the phase dependence of the optical bistability in the CQED system with the control of the magnetic field, and demonstrates that using magnetic field to manipulate light interference provides the possibility for active control of optical bistability. When the relative phase $\varphi = 0$ (the blue-dashed line), optical bistability can occur in the CQED system under the control of the magnetic field as shown in Figs. 11(c) and 11(d). When $\varphi = \pi/2$ (the red-dotted line and the purple-dash-dotted line), the CQED system operates in the monostable domain with the two different cavity-output powers. Furthermore, Fig. 11(d) shows that in the deep optical bistable domain the complicated bistable patterns can be obtained by tuning the phase φ to a different value. The CPA and optical bistability can be flexibly manipulated by controlling the magnetic field

and the relative phase between the two input light fields, which have practical applications in optical logic and optical communication devices. The nonlinear dependent relation between the cavity-output power and the cavity-input power is caused by the $|a|^2$-dependent nonlinear terms [Eqs. (32) and (33) are the quadratic equations of a]. The $|a|^2$-dependent nonlinear terms and phase modulation can lead to complicated bistable patterns in the deep optical bistable domain. For example, complicated bistable patterns can occur in the region of $1295 < P_{\text{in}} < 3130$ pW when $\varphi = \pi/2$ (the red-dotted line and the purple-dash-dotted line) in Fig. 11(d). In this region, it can be observed that the right cavity-output power P_{out}^r (the red-dotted line) and the left cavity-output power P_{out}^l (the purple-dash-dotted line) can be greater than the cavity-input power P_{in}. To illustrate that P_{out}^r and P_{out}^l cannot be greater than P_{in} at the same time, based on the parameters in Fig. 11(d), we plot $P_{\text{out}}^r/P_{\text{in}}$, $P_{\text{out}}^l/P_{\text{in}}$, and $P_{\text{out}}^t/P_{\text{in}}$ as a function of $|a|^2$ with $\varphi = \pi/2$ in Fig. 12. It is obvious from Fig. 12 that when P_{out}^r is greater than P_{in} ($P_{\text{out}}^r/P_{\text{in}} > 1$), P_{out}^l is less than P_{in} ($P_{\text{out}}^l/P_{\text{in}} < 1$), and vice versa. In the region of $1295 < P_{\text{in}} < 3130$ pW of Fig. 11(d), the number of intracavity photons $|a|^2$ corresponding to $P_{\text{out}}^r > P_{\text{in}}$ is different from $|a|^2$ corresponding to $P_{\text{out}}^l > P_{\text{in}}$. Figure 12 shows that P_{out}^r and P_{out}^l cannot be greater than P_{in} at the same time, and $P_{\text{out}}^t/P_{\text{in}} < 2$ also indicates that the total cavity-output power is not greater than the total cavity-input power.

The CPA and bistability of the CQED system sensitively depend on the cavity frequency detuning δ_c [see Eq. (35)]. We plot the two-dimensional map of $P_{\text{out}}/P_{\text{in}}$ as a function of P_{in} and δ_c/γ in Figs. 13(a) and 13(b) [corresponding to the three-dimensional plots of Figs. 13(c) and 13(d)], respectively. It can be clearly seen from Fig. 13 that the bistability of the CQED system depends on the cavity frequency detuning. By increasing the magnetic field, the absorption cavity-input power threshold (dark blue area) can be significantly increased in this CPA scheme based on the MIT configuration. The points marked in Figs. 13(a) and 13(c)
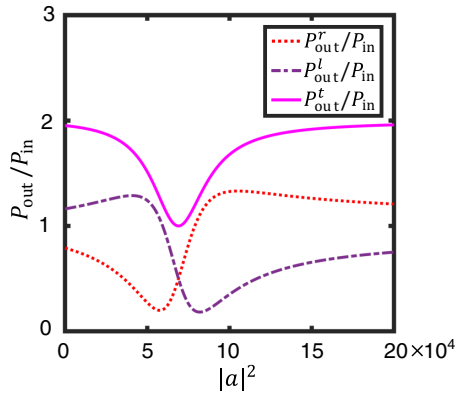
FIG. 12. The normalized cavity-output power P_{out}/P_{in} as a function of the number of intracavity photons $|a|^2$ with the relative phase $\varphi = \pi/2$. The normalized right cavity-output power P^r_{out}/P_{in} is denoted by the red-dotted line, the normalized left cavity-output power P^l_{out}/P_{in} is denoted by the purple-dash-dotted line, and the normalized total cavity-output power P^t_{out}/P_{in} ($P^t_{out} = P^r_{out} + P^l_{out}$) is denoted by the pink-solid line. The other parameters are $P^l_{in} = P^r_{in} = P_{in}$, $g\sqrt{N} = 15\gamma$, $\delta_c = 3.09\gamma$, $B = 4.5$ μT, $\kappa = 0.5\gamma$, $g = 0.02\gamma$, $T = 0.01$, and $\delta_p = \sqrt{2g^2N}$.

correspond well with the CPA point of the blue-dashed line in Fig. 11(d).
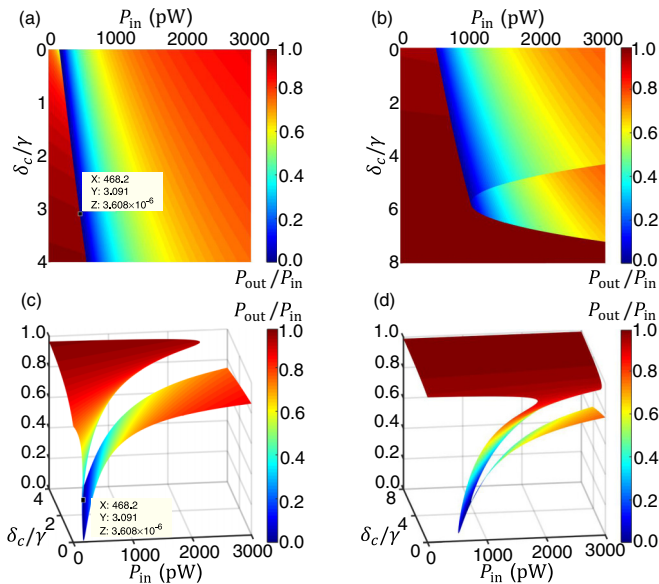

FIG. 13. (a) Contour plot of the normalized cavity-output power P_{out}/P_{in} as a function of the cavity-input power P_{in} as well as the cavity frequency detuning δ_c/γ with $B = 4.5$ μT. (b) Contour plot of the normalized cavity-output power P_{out}/P_{in} as a function of the cavity-input power P_{in} as well as the cavity frequency detuning δ_c/γ with $B = 7.5$ μT. The bottom panels (c) and (d) display the three-dimensional plots of the normalized cavity-output power P_{out}/P_{in} corresponding to the top panels (a) and (b), respectively. In order to better present the CPA characteristics of the CQED system, the coordinate axes of panels (a) and (b) are shown above. The points marked in panels (a) and (c) correspond to the CPA point in Fig. 11(d). The other parameters are $P^l_{in} = P^r_{in} = P_{in}$, $P^l_{out} = P^r_{out} = P_{out}$, $g\sqrt{N} = 15\gamma$, $\kappa = 0.5\gamma$, $g = 0.02\gamma$, $T = 0.01$, and $\delta_p = \sqrt{2g^2N}$.
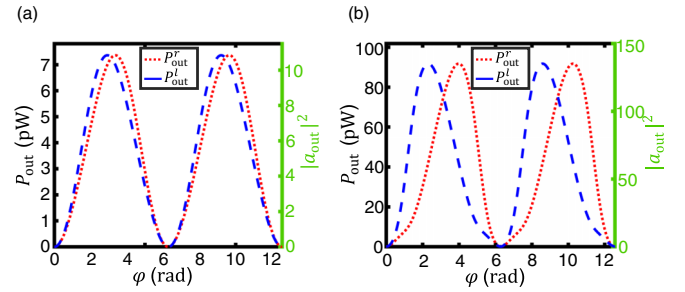

FIG. 14. With the cavity-input power below the threshold of the bistable domain, the right cavity-output power P^r_{out} (the red-dotted line) and the left cavity-output power P^l_{out} (the blue-dashed line) vs the relative phase φ between the two input light fields $a^r_{in} = |a^r_{in}|$ and $a^l_{in} = \alpha |a^r_{in}|e^{i\varphi}$. The right green vertical axis shows the output-light intensity $|a_{out}|^2$ in the CQED system. (a) $P_{in} = 7.3$ pW, $g\sqrt{N} = 10\gamma$, and $B = 1$ μT; (b) $P_{in} = 75.1$ pW, $g\sqrt{N} = 15\gamma$, and $B = 3$ μT. The other parameters are $P^l_{in} = P^r_{in} = P_{in}$, $\kappa = 0.5\gamma$, $g = 0.02\gamma$, $T = 0.01$, $\delta_p = \sqrt{2g^2N}$, and $\delta_c = 0$.

The closed-form formulas (32) and (33) show that the CPA can be manipulated by varying the relative phase φ between the two input light fields $a^r_{in} = |a^r_{in}|$ and $a^l_{in} = \alpha |a^r_{in}|e^{i\varphi}$. Figure 14 shows the two cavity-output powers P^r_{out} and P^l_{out} versus the relative phase φ with the CPA condition (34) satisfied, which demonstrates a detailed phase dependence of the CPA in the CQED system. The cavity-input power P_{in} in Fig. 14(a) ($P_{in} = 7.3$ pW) and Fig. 14(b) ($P_{in} = 75.1$ pW) is below the threshold for the onset of optical bistability. When the relative phase $\varphi = 0$ varies to $\varphi = \pi$, the system undergoes a transition from the CPA to high transmission (the two-side cavity-output power varies from zero to near the maximum value). When the CQED system is not in the strong nonlinear excitation regime at the lower cavity-input power, the phase dependence presents a nearly sinusoidal profile in Fig. 14(a). With the increase of cavity-input power, the CQED system is driven into the strong nonlinear excitation regime [still in the monostable domain; there is only one real solution from Eqs. (32) and (33)]. The phase dependence is distorted obviously from the sinusoidal behavior due to the nonlinearity, as shown in Fig. 14(b). The calculated phase dependence of the cavity-output power in the bistable domain behaves similarly to that in the monostable domain.

In order to more clearly show the influence of the system parameters on the transmission characteristics of the CQED system, we plot the two-dimensional color-scale map of the normalized cavity-output power P_{out}/P_{in} as a function of the cavity-input power P_{in} as well as the magnetic field B in Figs. 15(a) and 15(b). It can be clearly seen from Figs. 15(a) and 15(b) that the CPA and the nearly perfect photon absorption working window can appear in the case of weak cavity-input power, and the CPT can appear with the increase of the magnetic field in the system. The nearly perfect photon absorption working window can be broadened with the increase of the collective cavity-atom coupling strength $g\sqrt{N}$, which is consistent with Fig. 9(a). Figures 15(c) and 15(d) show the normalized cavity-output power P_{out}/P_{in} as a function of the cavity-input power P_{in} and the collective cavity-atom coupling strength $g\sqrt{N}/\gamma$. When the magnetic
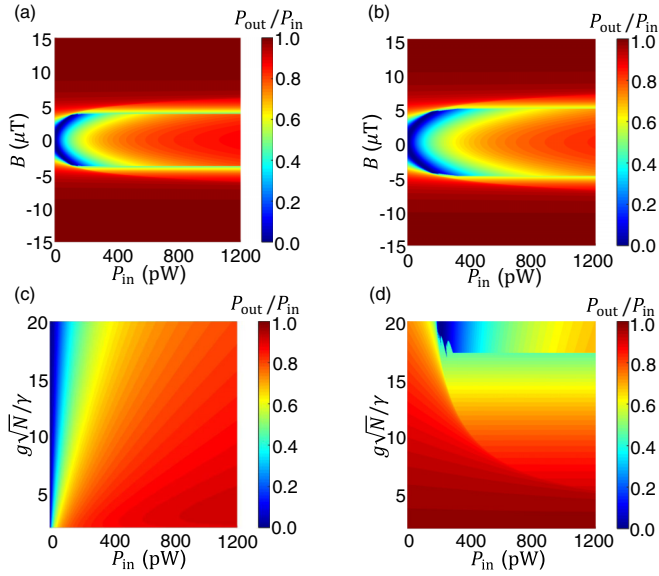
FIG. 15. (a) Contour plot of the normalized cavity-output power P_{out}/P_{in} as a function of the cavity-input power P_{in} as well as the magnetic field B with $g\sqrt{N} = 10\gamma$. (b) Contour plot of the normalized cavity-output power P_{out}/P_{in} as a function of the cavity-input power P_{in} as well as the magnetic field B with $g\sqrt{N} = 15\gamma$. (c) Contour plot of the normalized cavity-output power P_{out}/P_{in} as a function of the cavity-input power P_{in} as well as the collective cavity-atom coupling strength $g\sqrt{N}/\gamma$ with $B = 0$. (d) Contour plot of the normalized cavity-output power P_{out}/P_{in} as a function of the cavity-input power P_{in} as well as the collective cavity-atom coupling strength $g\sqrt{N}/\gamma$ with $B = 5$ μT. The other parameters are $P_{in}^l = P_{in}^r = P_{in}$, $P_{out}^l = P_{out}^r = P_{out}$, $\kappa = 0.5\gamma$, $g = 0.02\gamma$, $T = 0.01$, $\delta_p = \sqrt{2g^2N}$, and $\delta_c = 0$.

field $B = 0$ [see Fig. 15(c)], the CPA can occur at the weak cavity-input power. When the magnetic field $B = 5$ μT [see Fig. 15(d)], the CPA can appear at the strong cavity-input power. The dark blue area (i.e., the nearly perfect photon absorption) can increase slightly with the increase of $g\sqrt{N}$ in Fig. 15(c). However, the magnitude of this increase is much smaller than the change caused by the magnetic field in Fig. 15(d). The introduction of the magnetic field is beneficial for the absorption of stronger input lights in the CQED system.

Also, we plot the contour diagram showing P_{out}^r/P_{in} in Figs. 16(a) and 16(d), P_{out}^l/P_{in} in Figs. 16(b) and 16(e), and P_{out}^t/P_{in} in Figs. 16(c) and 16(f) with respect to the cavity-input power P_{in} and the relative phase φ. It is obvious that the pattern of the normalized right and left cavity-output power are symmetrically distributed. Through the pattern between the case without magnetic field [$B = 0$; see Figs. 16(a)–16(c)] and the case with applied magnetic field [$B = 3.5$ μT; see Figs. 16(d)–16(f)], it can be seen that under the control of the magnetic field [see Figs. 16(d) and 16(e)] the CPA can also appear in the case of the strong cavity-input power (the magnetic field makes the point of the CPA shift), which is a nonlinear effect. It can be noted from Figs. 16(a) and 16(b) and Figs. 16(d) and 16(e) that the normalized cavity-output power (P_{out}^r/P_{in} or P_{out}^l/P_{in}) can be greater than 1, which is

caused by the interference between the two input light fields under the applied magnetic field. Although the cavity-output power on one side of the cavity mirror can be greater than the cavity-input power ($P_{out}^r > P_{in}$ or $P_{out}^l > P_{in}$), the total cavity-output power is not greater than the total cavity-input power (the total cavity-output power is $2P_{in}$, i.e., the normalized total cavity-output power $P_{out}^t/P_{in} \leqslant 2$) [see Figs. 16(c) and 16(f)].

VI. CONCLUSIONS

In summary, we have investigated in detail a tunable CPA and CPT scheme in a cavity-atom structure with a single-mode cavity coupled to N three-level atoms under the static Faraday magnetic field. We find that the applied magnetic field plays an important role in modifying the photon output properties of the system. The input light fields coupled into the cavity can be completely absorbed or transmitted by turning the magnetic field on or off when it creates the cavity MIT, namely, controllable switching from CPA to CPT (or vice versa) can be achieved in such a system. We analyze the cavity input-output power relationships of the CQED system based on the MIT configuration coupled by two horizontally polarized input light fields from two opposite ends of the cavity in the linear and nonlinear excitation regimes. By tuning the magnetic field and altering the system parameters appropriately, the CPA can exist at different frequencies, which is different from the previous studies about CPA only for specific optical frequency. We also derive the approximate analytical solutions of the cavity-output power and the specific parameter matching conditions for the CPA. With the increase of the cavity-input power in the cavity, it is necessary to consider the nonlinearities as the atomic system is driven into the nonlinear excitation regime, especially if the light fields interfere constructively. In the nonlinear excitation regime, the CQED system with two input light fields can be driven into the bistable domain by the control of the magnetic field, and the CPA can persist when the cavity-input power is above the threshold value for optical bistability. In addition, the line shape and the threshold value for optical bistability can be flexibly controlled by varying the magnetic field and the relative phase of the two input fields under experimentally accessible conditions, and then optical bistability can be well tuned on or off. This well-tuned optical bistability facilitates the manipulation of the CPA. Also, we compare the analytical and numerical results of the cavity-output power in the nonlinear excitation regime, and they are in good agreement. Since the magnetic field can effectively control the CPA, this three-level excited CQED scheme based on the MIT configuration is suitable for future quantum light manipulation [37], absorptive switching [107], CPA-laser devices [23,108], quantum phase gates [109], etc.

Finally, it is worth pointing out that, according to the previous work [2], it is verified that tuning a system to a CPA in general is to move a zero of the elastic-scattering matrix onto the real wave-vector axis by introducing the appropriate dissipation to the system. In our present atom-cavity scheme, such an analysis about the motion of exact scattering-matrix zeros and poles in the complex-k plane, along the lines of Ref. [2], should also be made in principle and is left for further study.
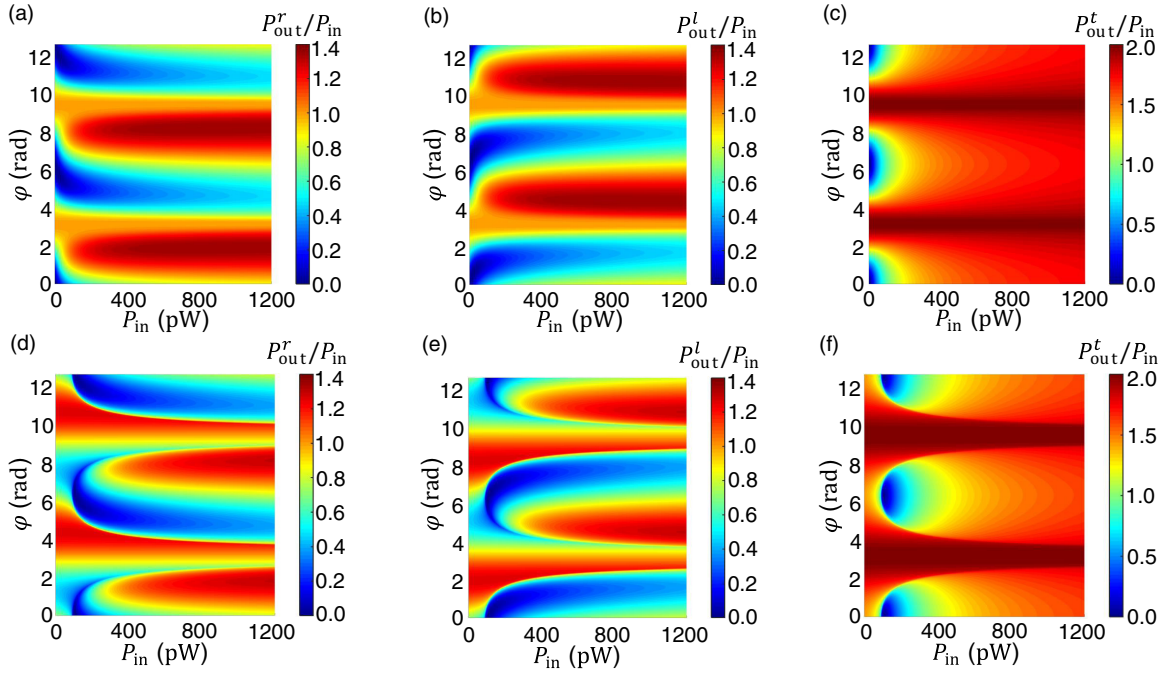
FIG. 16. Contour plot of (a) the normalized right cavity-output power $P_{\text{out}}^r/P_{\text{in}}$, (b) the normalized left cavity-output power $P_{\text{out}}^l/P_{\text{in}}$, and (c) the normalized total cavity-output power $P_{\text{out}}^t/P_{\text{in}}$ ($P_{\text{out}}^t = P_{\text{out}}^r + P_{\text{out}}^l$) as a function of the cavity-input power P_{in} as well as the relative phase φ between the two input light fields $a_{\text{in}}^r = |a_{\text{in}}^r|$ and $a_{\text{in}}^l = \alpha |a_{\text{in}}^r| e^{i\varphi}$ with $B = 0$. Contour plot of (d) the normalized right cavity-output power $P_{\text{out}}^r/P_{\text{in}}$, (e) the normalized left cavity-output power $P_{\text{out}}^l/P_{\text{in}}$, and (f) the normalized total cavity-output power $P_{\text{out}}^t/P_{\text{in}}$ as a function of the cavity-input power P_{in} as well as the relative phase φ with $B = 3.5$ μT. The other parameters are $P_{\text{in}}^l = P_{\text{in}}^r = P_{\text{in}}$, $g\sqrt{N} = 10\gamma$, $\kappa = 0.5\gamma$, $g = 0.02\gamma$, $T = 0.01$, $\delta_p = \sqrt{2g^2N}$, and $\delta_c = 0$.

[1] M. Born and E. Wolf, *Principles of Optics* (Cambridge University, Cambridge, England, 1999).

[2] Y. D. Chong, L. Ge, H. Cao, and A. D. Stone, Coherent Perfect Absorbers: Time-Reversed Lasers, Phys. Rev. Lett. **105**, 053901 (2010).

[3] W. J. Wan, Y. D. Chong, L. Ge, H. Noh, A. D. Stone, and H. Cao, Time-reversed lasing and interferometric control of absorption, Science **331**, 889 (2011).

[4] D. G. Baranov, A. Krasnok, T. Shegai, A. Alù, and Y. D. Chong, Coherent perfect absorbers: linear control of light with light, Nat. Rev. Mater. **2**, 17064 (2017).

[5] S. Dutta-Gupta, R. Deshmukh, A. V. Gopal, O. J. F. Martin, and S. D. Gupta, Coherent perfect absorption mediated anomalous reflection and refraction, Opt. Lett. **37**, 4452 (2012).

[6] H. M. Florez, L. S. Cruz, M. H. G. de Miranda, R. A. de Oliveira, J. W. R. Tabosa, M. Martinelli, and D. Felinto, Power-broadening-free correlation spectroscopy in cold atoms, Phys. Rev. A **88**, 033812 (2013).

[7] A. J. A. Carvalho, R. S. N. Moreira, J. Ferraz, S. S. Vianna, L. H. Acioli, and D. Felinto, Enhanced absorption of weak ultrashort light pulses by a narrowband atomic medium, Phys. Rev. A **101**, 053426 (2020).

[8] C. Q. Wang, W. R. Sweeney, A. D. Stone, and L. Yang, Coherent perfect absorption at an exceptional point, Science **373**, 1261 (2021).

[9] C. F. Gmachl, Suckers for light, Nature (London) **467**, 37 (2010).

[10] Y. H. Wei, W. J. Gu, G. Q. Yang, Y. F. Zhu, and G. X. Li, Coherent perfect absorption in a quantum nonlinear regime of cavity quantum electrodynamics, Phys. Rev. A **97**, 053825 (2018).

[11] W. Xiong, J. J. Chen, B. L. Fang, C. H. Lam, and J. Q. You, Coherent perfect absorption in a weakly coupled atom-cavity system, Phys. Rev. A **101**, 063822 (2020).

[12] L. Y. Wang, J. G. Hu, J. J. Du, and K. Di, Broadband coherent perfect absorption by cavity coupled to three-level atoms in linear and nonlinear regimes, New J. Phys. **23**, 123040 (2021).

[13] H. Noh, Y. D. Chong, A. D. Stone, and H. Cao, Perfect coupling of light to surface plasmons by coherent absorption, Phys. Rev. Lett. **108**, 186805 (2012).

[14] M. B. Pu, Q. Feng, M. Wang, C. G. Hu, C. Huang, X. L. Ma, Z. Y. Zhao, C. T. Wang, and X. G. Luo, Ultrathin broadband nearly perfect absorber with symmetrical coherent illumination, Opt. Express **20**, 2246 (2012).

[15] S. Feng and K. Halterman, Coherent perfect absorption in epsilon-near-zero metamaterials, Phys. Rev. B **86**, 165103 (2012).

[16] L. C. Botten, R. C. McPhedran, N. A. Nicorovici, and G. H. Derrick, Periodic models for thin optimal absorbers of electromagnetic radiation, Phys. Rev. B **55**, R16072 (1997).

[17] Y. Nakata, Y. Urade, T. Nakanishi, and M. Kitano, Plane-wave scattering by self-complementary metasurfaces in terms of electromagnetic duality and Babinet's principle, Phys. Rev. B **88**, 205138 (2013).

[18] C. Y. Huang, R. Zhang, J. L. Han, J. Zheng, and J. Q. Xu, Type-II perfect absorption and amplification modes with controllable bandwidth in combined $\mathcal{PT}$-symmetry and conventional Bragg-grating structures, Phys. Rev. A **89**, 023842 (2014).

[19] G. Pirruccio, L. M. Moreno, G. Lozano, and J. G. Rivas, Coherent and Broadband Enhanced Optical Absorption in Graphene, ACS Nano **7**, 4810 (2013).

[20] D. S. Hecht, L. B. Hu, and G. Irvin, Emerging transparent electrodes based on thin films of carbon nanotubes, graphene, and metallic nanostructures, Adv. Mater. **23**, 1482 (2011).

[21] S. Yu, X. J. Piao, J. H. Hong, and N. Park, Progress toward high-Q perfect absorption: A Fano antilaser, Phys. Rev. A **92**, 011802(R) (2015).

[22] J. H. Wu, M. Artoni, and G. C. L. Rocca, Perfect absorption and no reflection in disordered photonic crystals, Phys. Rev. A **95**, 053862 (2017).

[23] Y. D. Chong, L. Ge, and A. D. Stone, $\mathcal{PT}$-Symmetry Breaking and Laser-Absorber Modes in Optical Scattering Systems, Phys. Rev. Lett. **106**, 093902 (2011).

[24] Y. L. Liu, Q. C. Liu, S. P. Wang, Z. Chen, M. A. Sillanpää, and T. F. Li, Optomechanical Anti-Lasing with Infinite Group Delay at a Phase Singularity, Phys. Rev. Lett. **127**, 273603 (2021).

[25] G. Y. Nie, Q. C. Shi, Z. Zhu, and J. H. Shi, Selective coherent perfect absorption in metamaterials, Appl. Phys. Lett. **105**, 201909 (2014).

[26] M. Papaioannou, E. Plum, J. Valente, E. T. F. Rogers, and N. I. Zheludev, All-optical multichannel logic based on coherent perfect absorption in a plasmonic metamaterial, APL Photonics **1**, 090801 (2016).

[27] X. G. Hu, S. Yuan, A. Armghan, Y. Liu, C. Zeng, Z. Jiao, H. J. Lv, Y. Huang, Q. Z. Huang, Y. Wang, and J. S. Xia, A narrow-band coherent perfect absorption in bright-bright mode coupling metamaterials, J. Opt. **18**, 125101 (2016).

[28] A. Mostafazadeh and M. Sarisaman, Lasing-threshold condition for oblique TE and TM modes, spectral singularities, and coherent perfect absorption, Phys. Rev. A **91**, 043804 (2015).

[29] P. Bai, K. Ding, G. Wang, J. Luo, Z. Q. Zhang, C. T. Chan, Y. Wu, and Y. Lai, Simultaneous realization of a coherent perfect absorber and laser by zero-index media with both gain and loss, Phys. Rev. A **94**, 063841 (2016).

[30] S. Dutta-Gupta, O. J. F. Martin, S. D. Gupta, and G. S. Agarwal, Controllable coherent perfect absorption in a composite film, Opt. Express **20**, 1330 (2012).

[31] T. Y. Kim, M. A. Badsha, J. Yoon, S. Y. Lee, Y. C. Jun, and C. K. Hwangbo, General strategy for broadband coherent perfect absorption and multi-wavelength all-optical switching

based on epsilon-near-zero multilayer films, Sci. Rep. **6**, 22941 (2016).

[32] T. Roger, S. Vezzoli, E. Bolduc, J. Valente, J. J. F. Heitz, J. Jeffers, C. Soci, J. Leach, C. Couteau, N. I. Zheludev, and D. Faccio, Coherent perfect absorption in deeply subwavelength films in the single-photon regime, Nat. Commun. **6**, 7031 (2015).

[33] J. Yoon, M. Zhou, M. A. Badsha, T. Y. Kim, Y. C. Jun, and C. K. Hwangbo, Broadband epsilon-near-zero perfect absorption in the near-infrared, Sci. Rep. **5**, 12788 (2015).

[34] H. Park, S. Y. Lee, J. Kim, B. Lee, and H. Kim, Near-infrared coherent perfect absorption in plasmonic metal-insulator-metal waveguide, Opt. Express **23**, 24464 (2015).

[35] S. Mukherjee and S. D. Gupta, Coherent perfect absorption mediated enhancement of transverse spin in a gap plasmon guide, Eur. Phys. J. Appl. Phys. **76**, 30001 (2016).

[36] P. del Hougne, K. B. Yeo, P. Besnier, and M. Davy, Coherent Wave Control in Complex Media with Arbitrary Wavefronts, Phys. Rev. Lett. **126**, 193903 (2021).

[37] A. N. Vetlugin, Coherent perfect absorption of quantum light, Phys. Rev. A **104**, 013716 (2021).

[38] X. Fang, M. L. Tseng, J. Y. Ou, K. F. MacDonald, D. P. Tsai, and N. I. Zheludev, Ultrafast all-optical switching via coherent modulation of metamaterial absorption, Appl. Phys. Lett. **104**, 141102 (2014).

[39] X. Fang, K. F. MacDonald, and N. I. Zheludev, Controlling light with light using coherent metadevices: all-optical transistor, summator and invertor, Light Sci. Appl. **4**, e292 (2015).

[40] A. Xomalis, I. Demirtzioglou, E. Plum, Y. M. Jung, V. Nalla, C. Lacava, K. F. MacDonald, P. Petropoulos, D. J. Richardson, and N. I. Zheludev, Fibre-optic metadevice for all-optical signal modulation based on coherent absorption, Nat. Commun. **9**, 182 (2018).

[41] P. J. Wei, C. Croënne, S. T. Chu, and J. Li, Symmetrical and anti-symmetrical coherent perfect absorption for acoustic waves, Appl. Phys. Lett. **104**, 121902 (2014).

[42] T. Roger, S. Restuccia, A. Lyons, D. Giovannini, J. Romero, J. Jeffers, M. Padgett, and D. Faccio, Coherent Absorption of N00N States, Phys. Rev. Lett. **117**, 023601 (2016).

[43] A. H. M. Abdelaziz and A. K. Sarma, Effective control and switching of optical multistability in a three-level V-type atomic system, Phys. Rev. A **102**, 043719 (2020).

[44] M. Fleischhauer, A. Imamoglu, and J. P. Marangos, Electromagnetically induced transparency: Optics in coherent media, Rev. Mod. Phys. **77**, 633 (2005).

[45] Y. C. Liu, B. B. Li, and Y. F. Xiao, Electromagnetically induced transparency in optical microcavities, Nanophotonics **6**, 789 (2017).

[46] G. S. Agarwal and Y. F. Zhu, Photon trapping in cavity quantum electrodynamics, Phys. Rev. A **92**, 023824 (2015).

[47] G. S. Agarwal, K. Di, L. Y. Wang, and Y. F. Zhu, Perfect photon absorption in the nonlinear regime of cavity quantum electrodynamics, Phys. Rev. A **93**, 063805 (2016).

[48] L. Y. Wang, K. Di, Y. F. Zhu, and G. S. Agarwal, Interference control of perfect photon absorption in cavity quantum electrodynamics, Phys. Rev. A **95**, 013841 (2017).

[49] A. Sommer, Inducing transparency with a magnetic field, Physics **10**, 70 (2017).

[50] R. Gad, J. G. Leopold, A. Fisher, D. R. Fredkin, and A. Ron, Observation of Magnetically Induced Transparency in a

Classical Magnetized Plasma, Phys. Rev. Lett. **108**, 155003 (2012).

[51] X. Zhang, C. L. Zou, L. Jiang, and H. X. Tang, Strongly Coupled Magnons and Cavity Microwave Photons, Phys. Rev. Lett. **113**, 156401 (2014).

[52] G. H. Dong, D. Z. Xu, and P. Zhang, Magnetically induced optical transparency with an ultranarrow spectrum, Phys. Rev. A **102**, 033717 (2020).

[53] K. Ullah, M. T. Naseem, and Ö. E. Müstecaplıoğlu, Tunable multiwindow magnomechanically induced transparency, Fano resonances, and slow-to-fast light conversion, Phys. Rev. A **102**, 033721 (2020).

[54] A. H. Gevorgyan, Magnetically induced transparency in helically structured periodic crystals, Phys. Rev. E **105**, 014701 (2022).

[55] M. T. Cao, J. W. Wang, X. Yang, S. W. Qiu, H. Gao, and F. L. Li, Spatially modulated thermal light in atomic medium for enhanced ghost imaging, Sci. Rep. **7**, 8015 (2017).

[56] S. C. Bell, D. M. Heywood, J. D. White, J. D. Close, and R. E. Scholten, Laser frequency offset locking using electromagnetically induced transparency, Appl. Phys. Lett. **90**, 171120 (2007).

[57] O. Firstenberg, T. Peyronel, Q. Y. Liang, A. V. Gorshkov, M. D. Lukin, and V. Vuletić, Attractive photons in a quantum nonlinear medium, Nature (London) **502**, 71 (2013).

[58] R. Wynands and A. Nagel, Precision spectroscopy with coherent dark states, Appl. Phys. B **68**, 1 (1999).

[59] C. Liu, Z. Dutton, C. H. Behroozi, and L. V. Hau, Observation of coherent optical information storage in an atomic medium using halted light pulses, Nature (London) **409**, 490 (2001).

[60] T. Kessler, C. Hagemann, C. Grebing, T. Legero, U. Sterr, F. Riehle, M. Martin, L. Chen, and J. Ye, A sub-40-mHz-linewidth laser based on a silicon single-crystal optical cavity, Nat. Photonics **6**, 687 (2012).

[61] E. Abraham and S. D. Smith, Optical bistability and related devices, Rep. Prog. Phys. **45**, 815 (1982).

[62] J. Kerckhoff, M. A. Armen, D. S. Pavlichin, and H. Mabuchi, The dressed atom as binary phase modulator: towards atto-joule/edge optical phase-shift keying, Opt. Express **19**, 6478 (2011).

[63] A. Reiserer and G. Rempe, Cavity-based quantum networks with single atoms and optical photons, Rev. Mod. Phys. **87**, 1379 (2015).

[64] M. D. Guo, Quantum interference control of perfect photon absorption in a three-level atom-cavity system, Opt. Express **29**, 27653 (2021).

[65] J. W. Yoon, G. M. Koh, S. H. Song, and R. Magnusson, Measurement and Modeling of a Complete Optical Absorption and Scattering by Coherent Surface Plasmon-Polariton Excitation Using a Silver Thin-Film Grating, Phys. Rev. Lett. **109**, 257402 (2012).

[66] J. Jeffers, Nonlocal Coherent Perfect Absorption, Phys. Rev. Lett. **123**, 143602 (2019).

[67] Y. Sun, W. Tan, H. Q. Li, J. Li, and H. Chen, Experimental Demonstration of a Coherent Perfect Absorber with PT Phase Transition, Phys. Rev. Lett. **112**, 143903 (2014).

[68] S. Suwunnarat, D. Halpern, H. Li, B. Shapiro, and T. Kottos, Dynamically modulated perfect absorbers, Phys. Rev. A **99**, 013834 (2019).

[69] C. Schmidt, M. Sudzius, S. Meister, H. Fröb, and K. Leo, Controllable coherent absorption of counterpropagating laser beams in organic microcavities, Appl. Phys. Lett. **117**, 053301 (2020).

[70] S. Longhi, $\mathcal{PT}$-symmetric laser absorber, Phys. Rev. A **82**, 031801(R) (2010).

[71] W. R. Sweeney, C. W. Hsu, S. Rotter, and A. D. Stone, Perfectly Absorbing Exceptional Points and Chiral Absorbers, Phys. Rev. Lett. **122**, 093901 (2019).

[72] H. Y. Zheng, X. R. Jin, J. W. Park, Y. H. Lu, J. Y. Rhee, W. H. Jang, H. Cheong, and Y. P. Lee, Tunable dual-band perfect absorbers based on extraordinary optical transmission and Fabry-Perot cavity resonance, Opt. Express **20**, 24002 (2012).

[73] L. Chen, T. Kottos, and S. M. Anlage, Perfect absorption in complex scattering systems with or without hidden symmetries, Nat. Commun. **11**, 5826 (2020).

[74] M. N. Winchester, M. A. Norcia, J. R. K. Cline, and J. K. Thompson, Magnetically Induced Optical Transparency on a Forbidden Transition in Strontium for Cavity-Enhanced Spectroscopy, Phys. Rev. Lett. **118**, 263601 (2017).

[75] L. Y. Wang, Z. Tan, Y. F. Zhu, and M. S. Zhan, Control of optical bistability in the nonlinear regime of two-sided cavity quantum electrodynamics, J. Opt. Soc. Am. B **34**, 1780 (2017).

[76] M. O. Scully and M. S. Zubairy, *Quantum Optics* (Cambridge University, Cambridge, England, 1997).

[77] P. Meystre and M. Sargent, *Elements of Quantum Optics* (Springer-Verlag, Berlin, 2013).

[78] H. J. Carmichael, *Statistical Methods in Quantum Optics 1: Master Equations and Fokker-Planck Equations* (Springer, New York, 1999).

[79] G. S. Agarwal, *Quantum Optics* (Cambridge University, Cambridge, England, 2013).

[80] P. F. Yang, X. W. Xia, H. He, S. K. Li, X. Han, P. Zhang, G. Li, P. F. Zhang, J. P. Xu, Y. P. Yang, and T. C. Zhang, Realization of Nonlinear Optical Nonreciprocity on a Few-Photon Level Based on Atoms Strongly Coupled to an Asymmetric Cavity, Phys. Rev. Lett. **123**, 233604 (2019).

[81] L. Tang, J. S. Tang, M. Y. Chen, F. Nori, M. Xiao, and K. Y. Xia, Quantum Squeezing Induced Optical Nonreciprocity, Phys. Rev. Lett. **128**, 083604 (2022).

[82] X. W. Xia, X. Q. Zhang, J. P. Xu, H. Z. Li, Z. Y. Fu, and Y. P. Yang, Giant nonreciprocal unconventional photon blockade with a single atom in an asymmetric cavity, Phys. Rev. A **104**, 063713 (2021).

[83] J. H. Li, Y. Qu, R. Yu, and Y. Wu, Generation and control of optical frequency combs using cavity electromagnetically induced transparency, Phys. Rev. A **97**, 023826 (2018).

[84] C. Dong, V. Fiore, M. C. Kuzyk, and H. Wang, Optomechanical dark mode, Science **338**, 1609 (2012).

[85] J. K. Stockton and A. K. Tuchman, Quantum limits and robustness of nonlinear intracavity absorption spectroscopy, Phys. Rev. A **79**, 013822 (2009).

[86] T. H. Loftus, T. Ido, A. D. Ludlow, M. M. Boyd, and J. Ye, Narrow Line Cooling: Finite Photon Recoil Dynamics, Phys. Rev. Lett. **93**, 073003 (2004).

[87] A. Derevianko and H. Katori, Colloquium: Physics of optical lattice clocks, Rev. Mod. Phys. **83**, 331 (2011).

[88] M. A. Norcia, M. N. Winchester, J. R. K. Cline, and J. K. Thompson, Superradiance on the millihertz linewidth strontium clock transition, Sci. Adv. **2**, e1601231 (2016).

[89] M. A. Norcia and J. K. Thompson, Cold-Strontium Laser in the Superradiant Crossover Regime, Phys. Rev. X **6**, 011025 (2016).

[90] M. A. Norcia and J. K. Thompson, Strong coupling on a forbidden transition in strontium and nondestructive atom counting, Phys. Rev. A **93**, 023804 (2016).

[91] K. Pandey, C. C. Kwong, M. S. Pramod, and D. Wilkowski, Linear and nonlinear magneto-optical rotation on the narrow strontium intercombination line, Phys. Rev. A **93**, 053428 (2016).

[92] A. J. Heinrich, J. A. Gupta, C. P. Lutz, and D. M. Eigler, Single-atom spin-flip spectroscopy, Science **306**, 466 (2004).

[93] G. S. Pati, R. Tripathi, R. S. Grewal, M. Pulido, and R. A. Depto, Synchronous coherent population trapping and its magnetic spectral response in rubidium vapor, Phys. Rev. A **104**, 033116 (2021).

[94] D. Lombardo and J. Twamley, Deterministic creation of macroscopic cat states, Sci. Rep. **5**, 13884 (2015).

[95] K. A. Yasir and W. M. Liu, Controlled electromagnetically induced transparency and fano resonances in hybrid BEC-optomechanics, Sci. Rep. **6**, 22651 (2016).

[96] J. Klinder, H. Keßler, C. Georges, J. Vargas, and A. Hemmerich, Bose-Einstein condensates in an optical cavity with sub-recoil bandwidth, Appl. Phys. B **122**, 299 (2016).

[97] G. Chimczak, K. Bartkiewicz, Z. Ficek, and R. Tanaś, Creating a switchable optical cavity with controllable quantum-state mapping between two modes, Sci. Rep. **8**, 14740 (2018).

[98] L. Kohler, M. Mader, C. Kern, M. Wegener, and D. Hunger, Tracking Brownian motion in three dimensions and characterization of individual nanoparticles using a fiber-based high-finesse microcavity, Nat. Commun. **12**, 6385 (2021).

[99] K. Kustura, C. G. Ballestero, A. d. l. R. Sommer, N. Meyer, R. Quidant, and O. R. Isart, Mechanical Squeezing via Unstable Dynamics in a Microcavity, Phys. Rev. Lett. **128**, 143601 (2022).

[100] H. Keßler, J. Klinder, M. Wolke, and A. Hemmerich, Steering Matter Wave Superradiance with an Ultranarrow-Band Optical Cavity, Phys. Rev. Lett. **113**, 070404 (2014).

[101] M. Khudaverdyan, W. Alt, I. Dotsenko, T. Kampschulte, K. Lenhard, A. Rauschenbeutel, S. Reick, K. Schörner, A. Widera, and D. Meschede, Controlled insertion and retrieval of atoms coupled to a high-finesse optical resonator, New J. Phys. **10**, 073023 (2008).

[102] S. Dutta and S. A. Rangwala, All-optical switching in a continuously operated and strongly coupled atom-cavity system, Appl. Phys. Lett. **110**, 121107 (2017).

[103] H. Primakoff and T. Holstein, Many-body interactions in atomic and nuclear systems, Phys. Rev. **55**, 1218 (1939).

[104] J. Petersen, J. Volz, and A. Rauschenbeutel, Chiral nanophotonic waveguide interface based on spin-orbitinteraction of light, Science **346**, 67 (2014).

[105] I. M. Mirza and J. C. Schotland, Multiqubit entanglement in bidirectional-chiral-waveguide QED, Phys. Rev. A **94**, 012302 (2016).

[106] A. Kuhn, *Engineering the Atom-Photon Interaction* (Springer-Verlag, Berlin, 2015).

[107] C. J. Min and G. Veronis, Absorption switches in metal-dielectric-metal plasmonic waveguides, Opt. Express **17**, 10757 (2009).

[108] Z. J. Wong, Y. L. Xu, J. Kim, K. O'Brien, Y. Wang, L. Feng, and X. Zhang, Lasing and anti-lasing in a single cavity, Nat. Photonics **10**, 796 (2016).

[109] R. García-Maraver, R. Corbalán, K. Eckert, S. Rebić, M. Artoni, and J. Mompart, Cavity QED quantum phase gates for a single longitudinal mode of the intracavity field, Phys. Rev. A **70**, 062324 (2004).